Geophysical Journal International

Geophys. J. Int. (2026) **245,** 1–21
Advance Access publication 2026 January 28
Research Paper

https://doi.org/10.1093/gji/ggag040

Constraining time-lapse geophysical responses with reactive transport modelling: an approach to monitor H_2S mineral storage

Daniel A. Ciraula [1], Gianluca Fiandaca [2], Jian Chen [2], Samuel Scott [1] and Léa Lévy [3]

[1] *NordVulk, Institute of Earth Sciences, University of Iceland,* 101 *Reykjavík, Iceland. Email: danielac@hi.is*
[2] *Department of Earth Sciences "Ardito Desio", University of Milano,* 20133 *Milano, Italy*
[3] *University of Rennes, CNRS-INSU, Géosciences Rennes, UMR* 6118, 35000 *Rennes, France*

Accepted 2025 December 19. Received 2025 November 7; in original form 2025 June 30

SUMMARY

Geothermal energy production emits significant amounts of hydrogen sulfide (H_2S). A strategy to mitigate the emissions is to reinject the H_2S into basaltic formations, where it reacts with the rock to form pyrite. Due to the polarization properties of pyrite, the direct current resistivity (DC) and induced polarization (IP) geophysical method (i.e. DCIP) has shown the potential for monitoring H_2S mineral storage. However, field applications of DCIP monitoring have been limited by the low spatial coverage of wireline logging and by the ambiguity in interpreting IP signals due to multiple processes that contribute to the polarization response. This study integrates DCIP with field-scale reactive transport modelling, utilizing both synthetic modelling and field investigations, to assess the ability of surface and cross-hole DCIP to monitor H_2S mineral storage at the Nesjavellir study site in Iceland. Two surface DCIP data sets were collected at Nesjavellir, with six months of continuous H_2S injection between them. Time-lapse inversions, performed using a novel gridding scheme that accounts for electrode misplacement between the two DCIP surveys, recover no significant IP changes beyond data noise. Interpreting these results alongside the reactive transport results finds that pyrite mineralization during the six-month injection period is too small and too deep to be resolved by surface DCIP time-lapse surveying, highlighting the benefit of a joint geophysical–geochemical interpretation approach. Conversely, joint DCIP-reactive transport synthetic modelling shows the potential of cross-hole DCIP for monitoring long-term H_2S mineral storage, provided that data noise is low and sufficient H_2S is injected. The reactive transport models also provide insight into the mechanisms contributing to the polarization response, demonstrating that pyrite mineralization is the primary contributor to the polarization response, with minimal contribution from other minerals such as smectites and iron oxides. However, existing petrophysical relationships are simplistic, which adds uncertainty to the interpretation of the DCIP signal and the quantification of pyrite mineralization. Additionally, smectite formation has been shown to decrease both the polarization signals and the quality of the IP data due to its electrically conductive properties. At Nesjavellir, a decrease in the DC resistivity from 1925 to 325 Ωm is observed, attributed to the disposal of warm wastewater. This decrease is identified by comparing resistivity data collected in this study to historical vertical electrical sounding data collected prior to geothermal development. Lastly, petrophysical relationships linking DC resistivity, smectite content and permeability suggest a high basalt fracture permeability of 7.9×10^{-12} m^2, which agrees with values recovered through flow model calibrations. This result demonstrates the value of geophysical surveying not only for monitoring but also for constraining key parameters in reactive transport simulations.

Key words: Induced polarization; Inverse theory; Hydrogeophysics; Hydrothermal systems.

1 INTRODUCTION

Geothermal energy is a key component of the Icelandic energy grid, accounting for 65 per cent of the nation's electricity and heating production (Government of Iceland 2016). While geothermal energy provides a stable and clean source of energy, the flash steam geothermal production in Iceland emits roughly 30 000 tons of H_2S per year (C. Marieni *et al.* 2018). These gases are naturally occurring in the high-enthalpy geothermal production fluids, where concentrations are generally in the hundreds of parts per million (S. Arnórsson 1995; I.M. Galeczka *et al.* 2022). H_2S gases are toxic to humans and the environment, and their emissions are regulated within Iceland (Government of Iceland 2010).

To reduce H_2S emissions from geothermal energy production, gas is dissolved into geothermal wastewater and injected into the subsurface in a mineral storage sequestration approach. Upon injection, the H_2S-charged wastewater interacts with the basaltic host reservoir, binding fluid-sourced sulfide with iron released upon basalt alteration to mineralize iron sulfides (e.g. pyrite).

Geochemical models, laboratory experiments and field geochemical sampling indicate that this H_2S mineral storage approach in basalts is an effective method to reduce atmospheric H_2S emissions (A. Stefánsson *et al.* 2011; S.O. Snæbjörnsdóttir *et al.* 2017; D.E. Clark *et al.* 2018, 2020; J. Prikryl *et al.* 2018; C. Marieni *et al.* 2021; S.O. Snæbjörnsdóttir *et al.* 2021; I.M. Galeczka *et al.* 2022; D.A. Ciraula *et al.* 2024). However, the H_2S injection system must be monitored to mitigate potential environmental impacts, including groundwater acidification, chemical and thermal contamination of fresh surface and water systems and pore-clogging of the storage reservoir (B. Callow *et al.* 2018; D.A. Ciraula *et al.* 2024). Current monitoring approaches are primarily limited to geochemical approaches with low spatial resolution, such as mass balance calculations based on fluid sampling of monitoring wells (J.M. Matter *et al.* 2016; S.O. Snæbjörnsdóttir *et al.* 2017; I. Gunnarsson *et al.* 2018; D.E. Clark *et al.* 2020).

Geophysical surveying, aided by recent advancements in data acquisition and time-lapse inversion software, has been established as a reliable tool to improve the spatial and temporal resolution of environmental monitoring efforts (e.g. A. Binley *et al.* 2015; K. Singha *et al.* 2015). Electrical geophysical methods have been particularly beneficial for hydrological and environmental monitoring due to their sensitivity to relevant hydrogeological parameters, such as pore fluid conductivity, pore space geometry, and electrochemical interactions at the fluid–rock interface (K. Singha *et al.* 2015). By constraining these parameters, electrical geophysical data can be integrated with process-based models, such as flow and transport models and reactive transport models, to assist in hydrogeological mapping (S. Üner *et al.* 2019), hydrological parameter estimation (e.g. T.D. Scheibe & Y.J. Chien 2003; R. Deiana *et al.* 2008; A.C. Hinnell *et al.* 2010; D. Pollock & O.A. Cirpka 2012; M. Camporese *et al.* 2015; A.P. Tran *et al.* 2016; M. Commer *et al.* 2020; S.Y. Cheng & Hsu 2021; M.S. Pleasants *et al.* 2022) and hydrological monitoring (e.g. A. Kemna *et al.* 2002; Y. Rubin & S.S. Hubbard 2005; A. Flores-Orozco *et al.* 2011; M.A. Briggs *et al.* 2013; J. Chen *et al.* 2013). Likewise, process-based models can provide information on geophysical inversion parameters (e.g. M. Commer *et al.* 2022) and the underlying processes controlling the geophysical response (e.g. Y. Wu *et al.* 2011; B. Ahmmed *et al.* 2020). Therefore, integrating the two approaches presents a mutual benefit between the geophysical methods and process-based models (Y. Wu *et al.* 2014).

Induced polarization (IP) is an electrical geophysical method that measures the transfer and reversible accumulation of charges in a porous medium (e.g. J. Wong 1979; A. Revil *et al.* 2015). The IP method is sensitive to multiple reactive processes, making it a potentially powerful tool for monitoring environmental applications (e.g. L.D. Slater & D. Lesmes 2002; P. Kessouri *et al.* 2019), including secondary mineral precipitation associated with bioremediation (e.g. D. Ntarlagiannis *et al.* 2005; K.H. Williams *et al.* 2005, 2009; A. Flores-Orozco *et al.* 2011, 2013), microbially induced calcite precipitation (e.g. Y. Wu *et al.* 2011; S. Saneiyan *et al.* 2018, 2019), geothermal alteration (e.g. A. Revil *et al.* 2017b; A. Ghorbani *et al.* 2018; A. Revil & M. Gresse 2021) and mineral storage approaches (e.g. D.A. Ciraula *et al.* 2024; L. Lévy *et al.* 2024b). However, the IP signature is often a result of confounding processes, leading to ambiguity in the interpretation of the complex IP response. As detailed in P. Kessouri *et al.* (2019), a growing number of laboratory studies have integrated IP with reactive models (e.g. reactive experiments and numerical simulations) to help de-couple the underlying reactive processes. Critically, these studies have found that integrating IP with reactive models serves to monitor the rates of reactive processes (K.H. Williams *et al.* 2005; S. Saneiyan *et al.* 2018; A. Mellage *et al.* 2018b), enhance the conceptual understanding of the reactions (Y. Wu *et al.* 2010; A. Mellage *et al.* 2018b; F. Rembert 2021), constrain hydrogeologic parameters essential for numerical modelling (Y. Wu *et al.* 2014) and deconvolve the multiple contributions to the measured IP signal (Y. Wu *et al.* 2010, 2011; C.G. Hubbard *et al.* 2013; A. Mellage *et al.* 2018a, b; K. Peshtani *et al.* 2025).

While integrating IP with reaction models has shown utility in laboratory settings, the integration of IP surveying with reactive models in the field remains underutilized (P. Kessouri *et al.* 2019). For example, K.H. Williams *et al.* (2009) corroborated the field IP bioremediation monitoring surveys with laboratory column experiments and analysis of fluids and sediments to attribute the IP response to iron and sulfate reduction and identify other IP mechanisms to investigate in future work. S. Saneiyan *et al.* (2019) combined geochemical monitoring and laboratory sample analyses with field IP data to monitor microbially induced carbonate precipitation. More recently, and of particular relevance to the work presented here, D.A. Ciraula *et al.* (2024) integrated reactive transport modelling with the direct current resistivity (DC) and time-domain IP electrical methods, commonly referred to together as DCIP, to evaluate pyrite formation in field-scale H_2S mineral storage. The semiconducting properties of pyrite generates a strong IP response which can indicate alteration zones and provide a direct measure of H_2S mineralization (D.A. Ciraula *et al.* 2024; L. Lévy *et al.* 2024b). Through qualitative integration of wireline DCIP with reactive transport modelling, D.A. Ciraula *et al.* (2024) identified the key hydrogeological parameters (i.e. porosity, permeability, temperature and injection rate) controlling the degree of pyrite mineralization and its associated DCIP response. However, L. Lévy *et al.* (2024b) brought into question the long-term stability of H_2S mineral storage at Nesjavellir and highlighted further ambiguities in the interpretation of the IP changes. Additionally, the wireline DCIP logging survey

provided limited spatial extent for monitoring H_2S mineralization.

This study quantitatively integrates time-lapse DCIP geophysics with field-scale reactive transport models to better characterize H_2S mineralization at the Nesjavellir injection site in SW Iceland. We utilize a novel time-lapse inversion software and flexible gridding approach to recover changes in full waveform, surface DCIP data collected at Nesjavellir in 2020, prior to H_2S injection, and in 2021 following six months of continuous H_2S injection. We compare the time-lapse inversion results to the expected DCIP changes from reactive transport simulations in a joint approach to constrain interpretations of the H_2S mineral storage. The reactive transport models are also used for joint geochemical–geophysical synthetic modelling to evaluate the cross-hole DCIP survey configuration, enhancing the monitoring of H_2S mineral storage at the Nesjavellir site. Lastly, reactive transport models are utilized alongside historical electric geophysical data to better understand the underlying processes contributing to the DCIP response associated with H_2S mineral storage. Specifically, there are three main aims of this study: (1) evaluate the ability of DCIP to monitor H_2S mineral storage through field surveying and joint reactive transport-DCIP synthetic modelling; (2) reduce ambiguity in geophysical DCIP interpretations by constraining the underlying processes contributing to geophysical responses; (3) explore how time-lapse DCIP can be used to validate reactive transport model parameters.

2 DCIP GEOPHYSICS BACKGROUND

2.1 DCIP Methodology

The DCIP method expands upon the Ohmic conduction measured in conventional DC electrical resistivity surveys by considering induced polarization (IP), a low-frequency capacitive effect in the subsurface (e.g. W.H. Pelton *et al.* 1978; J. Wong 1979; D.P. Lesmes & K.M. Frye 2001). IP describes the ability of a material to store electrical charges, and the response is largely driven by the reorganization of charges of the electrical double layer at the pore fluid–rock interface during the current injection (e.g. R.T. Shuey 1975; H.J. Vinegar & Waxman 1984; M. Bücker *et al.* 2018). The IP effect is frequency-dependent; thus, IP considers a complex resistivity that is the sum of the real (ρ') and imaginary (ρ'') parts of resistivity (e.g. G. Fiandaca *et al.* 2015b):

$$\rho^* = \rho' + i\rho'' \,. \tag{1}$$

This study utilizes time-domain IP, where a sequence of direct current pulses of alternating polarity is injected through two grounded electrodes (A and B) to build up charge in the subsurface. The build-up of charges creates a time-dependent voltage that is measured at two additional electrodes (M and N). The current and voltage electrodes are commonly placed along lines at the surface (surface DCIP) or down neighbouring boreholes (cross-hole DCIP). In both the surface and cross-hole DCIP approaches, the A-B-N-M electrodes make up a single quadrapole and represent a single geoelectrical measurement called the complex apparent resistivity (ρ_a^*) (T. Martin *et al.* 2021):

$$\rho_a^* = k \times \frac{2\pi\,\Delta V_{\mathrm{MN}}^*}{I^*} \,, \tag{2}$$

where ΔV_{MN}^* is the measured time-varying voltage difference between the M and N electrodes and I^* is the time-varying current injected. The term k is a geometric factor related to the distances between the various electrodes (AM, AM, BM, BN), defined as:

$$k = \frac{1}{\frac{1}{\mathrm{AM}} - \frac{1}{\mathrm{AN}} - \frac{1}{\mathrm{BM}} + \frac{1}{\mathrm{BN}}} \,. \tag{3}$$

The time-varying voltage response between the M and N electrodes (ΔV_{MN}^*) contains the static (DC) voltage response and an IP voltage response which arises as residual charges, accumulated during current injection, return to equilibrium (voltage decay). In this study, we use a 100 per cent duty-cycle with no off-time between the injection current polarity switch (P.I. Olsson *et al.* 2015). The 100 per cent duty-cycle ($+I_{\mathrm{on}}, -I_{\mathrm{on}}$) is preferred in this study over the 50 per cent duty-cycle ($+I_{\mathrm{on}}, I_{\mathrm{off}}, -I_{\mathrm{on}}, I_{\mathrm{off}}$) because data acquisition is twice as fast and the signal strength is approximately doubled (P.I. Olsson *et al.* 2015).

2.2 IP relaxation model

A common relaxation model used to describe the IP voltage response curve is the complex resistivity Cole–Cole model (W.H. Pelton *et al.* 1978; A. Weller & L. Slater 2022). The Cole–Cole model describing complex resistivity (RCC) can be defined by the resistivity (ρ_0), chargeability (m), relaxation time (τ_σ) and frequency exponent (C):

$$\mathrm{RCC}\{\rho_0, m, \tau_\sigma, C\} = \rho_0 \left[1 - m\left(1 - \frac{1}{1 + (i\omega\tau_\sigma)^C}\right)\right] . \tag{4}$$

In this study, we invert the complex resistivity for maximum phase angle model parameters (MPA) (G. Fiandaca *et al.* 2018), a re-parametrization of the RCC model. We utilize this re-parametrization as it has been shown to decrease model parameter correlation and improve model resolution, particularly in data with low signal-to-noise ratios (G. Fiandaca *et al.* 2018). In the MPA model, the model domain is re-parametrized to MPA $\{\rho_0, \phi_{\max}, \tau_\phi, C\}$. The relaxation time, τ_ϕ, is defined in terms of the Cole–Cole parameters m, τ_ϕ and C:

$$\tau_\phi = \tau_\sigma \times (1 - m)^{-1/2C} \,. \tag{5}$$

The phase of the Cole–Cole complex resistivity, $\phi(\omega)$, is maximized at an angular frequency of $\omega_\phi = 1/\tau_\phi$. Thus, the maximum phase, $\phi_{\max}$, can be described as:

$$\phi_{\max} = -\tan^{-1}\left(\frac{\rho''(1/\tau_\phi)}{\rho'(1/\tau_\phi)}\right) . \tag{6}$$

After the inversion, we calculate the RCC parameters from the MPA parameters following the iterative approach outlined in appendix A of Fiandaca et al. (2018). The routine calculates the chargeability m by matching the phase reponse of the MPA and RCC models; $m = \frac{\tan(-\phi_{\max})}{(1-a)\cdot\tan(-\phi_{\max})+b}$, where a and b are the real and imaginary part of $\frac{1}{1+(i\omega\tau_\rho)^C}$, calculated at the frequency $\omega = \frac{1}{\tau_\phi}$ at which the maximum phase is reached. The chargeability m and relaxation time τ_ρ are computed iteratively through these equations using the relation $\tau_\rho = \tau_\phi \cdot (1 - m)^{-1/2C}$, starting with $m = 0$ and $\tau_\rho = \tau_\phi$ and minimizing $\Delta m = \frac{|m(n) - m(n-1)|}{m(n)}$ over n iterations. This procedure yields the RCC parameter set, including the chargeability used in the petrophysical relationship discussed in the following section.

2.3 Petrophysical IP relationship

It is well established that disseminated metallic minerals, such as iron sulfides and some iron oxides, have a large impact on the polarization characteristics of the subsurface (e.g. J. Wong 1979; G. Gurin *et al.* 2013, 2015; A. Revil *et al.* 2015; S. Hupfer *et al.* 2016; F. Abdulsamad *et al.* 2017). A. Revil *et al.* (2015) presents a polarization model for disseminated metallic particles, based on the effective medium theory, where the semiconducting properties of metallic minerals allow for electron mobility within the minerals themselves, accumulating additional charge at the mineral-electrolyte interface when an external electric field is applied. The model from A. Revil *et al.* (2015) used in this study follows a similar approach to the models produced in J. Wong (1979) and G. Gurin *et al.* (2015), relating the the chargeability parameter, m, to the sum of the background chargeability (m_b) and the volume fraction of semiconducting metallic particles in the porous media, θ_{metallic}:

$$m = \frac{9}{2} \times \theta_{\text{metallic}} + m_b \,. \tag{7}$$

Analysis of core samples of altered Icelandic volcanic rocks in L. Lévy *et al.* (2019a) confirmed the linear relationship between the IP response and the volume content of metallic particles, thereby supporting the use of eq. (7) to serve as a first-order approximation to link H_2S mineralization to the expected chargeability response.

A. Ghorbani *et al.* (2018) shows that the background chargeability term (m_b) is constant when fluid salinity is low, independent of temperature and saturation. Additionally, the metallic minerals are comprised of iron oxides and iron sulfides, which are expected to have similar influences on the chargeability based on derivations of the chargeability from the effective medium theory (A. Revil *et al.* 2015). Similarly, laboratory studies of sand-metallic particle mixtures in G. Gurin *et al.* (2015) found that the mineral composition has minimal impact on chargeability. Therefore, the chargeability change simplifies to reflect only the change in volume fraction of iron sulfides (pyrite and pyrrhotite) from precipitation and primary iron oxides (magnetite and ilmenite) from dissolution:

$$\Delta m = \frac{9}{2} \times (\Delta\theta_{\text{iron-sulfides}} + \Delta\theta_{\text{iron-oxides}}) \,. \tag{8}$$

Chargeability in eq. (8) is not anticipated to be influenced by temperature, as it depends on the ratio of high-frequency conductivity to direct current conductivity, which shares the same temperature relationship (A. Ghorbani *et al.* 2018). Fluid conductivity effects are also not considered in eq. (8) as previous studies have shown that chargeability is independent of the pore fluid conductivity over a similar range of values as observed at Nesjavellir (~0.01–0.07 S m^{-1}) (G. Gurin *et al.* 2015; S. Hupfer *et al.* 2016; L. Lévy *et al.* 2019a). Furthermore, major temperature and fluid conductivity changes between the time-lapse measurements are not expected as hot wastewater injection began at Nesjavellir two decades before introducing H_2S.

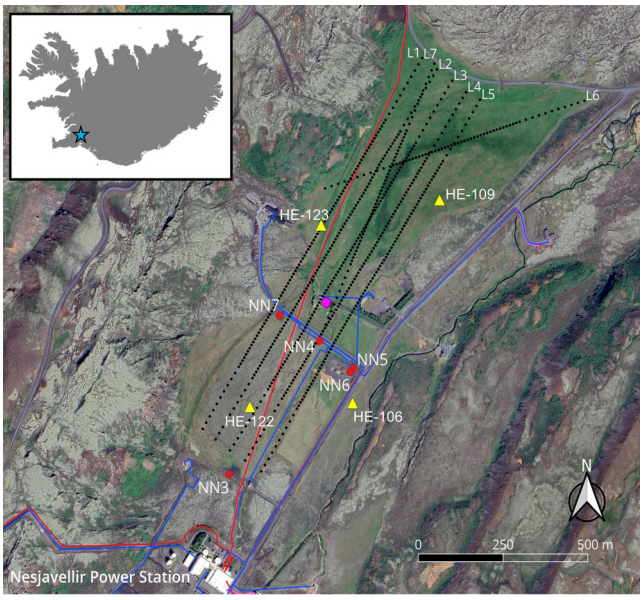

Figure 1. Map of the Nesjavellir geothermal field site. The H_2S injection wells are shown as red circles. The approximate electrode locations along the DCIP survey lines are displayed as black dots and the locations of the vertical electrical soundings collected in 1985 are shown as yellow triangles. Red lines indicate buried power lines, the pink square is the location of a residential building and the blue lines indicate hot water and steam pipes.

3 METHODS

3.1 DCIP field data

3.1.1 Nesjavellir field site

The data set used to test the DCIP monitoring approach developed in this paper was collected at the Nesjavellir high-temperature geothermal field. Nesjavellir is located north of the Hengill central volcano in southwest Iceland, situated on a ridge–ridge-transform triple junction (G.R. Foulger 1988). The area is composed mainly of late Quaternary and post-glacial age volcanic rocks, primarily in basalt lava flows and hyaloclastites (B. Arnason *et al.* 1969; G.R. Foulger & D.R. Toomey 1989).

The power plant produces 120 MWe of electricity and 290 MWth as thermal energy for district heating (E. Gómez-Díaz *et al.* 2022). Since 2004, warm geothermal wastewater produced as a byproduct of energy production has been injected into shallow wells ('NN wells', 200–500 m deep) or discharged at the surface into ~25 m deep wells near the power plant and into a nearby disappearing stream. At the NN well injection depths, the groundwater system is cold (10 °C) and the basalt is unaltered, comprised of highly porous and permeable hyaloclastites and basalt lava flows (H.M. Helgadóttir 2021; E. Gómez-Díaz *et al.* 2022; D.A. Ciraula *et al.* 2024). The groundwater table is measured at 50–60 m depth.

Starting 2021 January 29, H_2S from the geothermal production fluid is dissolved into the geothermal wastewater and injected into the NN wells located 250–750 m northeast of the Nesjavellir power station (Fig. 1). The injection water temperature ranges from 60 °C to 90 °C and H_2S concentrations are ~75 ppm. Injection is continuous at each well at rates ranging from 15 to 150 L s^{-1}. Additional information on the Nesjavellir geothermal

site can be found in L. Lévy *et al.* (2024b) and D.A. Ciraula *et al.* (2024).

3.1.2 Time-lapse DCIP data acquisition during H_2S injection

Time-domain, full waveform surface DCIP data were acquired at the Nesjavellir field site in July 2020 and 2021 (Fig. 1) using the ABEM Terrameter LS2 with a maximum injection current of 500 mA at 600 V. In the field, injection currents averaged ∼350 mA. Stainless steel electrodes were used in this survey, which can introduce background drift to the data due to the electrochemical and current-induced electrode polarization of the stainless steel electrodes (e.g. T. Dahlin *et al.* 2002; P.I. Olsson *et al.* 2016). However, we utilize the full-waveform drift model presented in P.I. Olsson *et al.* (2016), which has been shown to effectively remove the background drift from data collected with stainless steel electrodes. Data were collected along seven survey lines in both years with a multiple gradient array acquisition. Five of the lines, Lines 1–5, were 1200 m long and oriented at roughly 33°E of N, parallel to the Nesjavellir rift valley and along the principal direction of groundwater flow. The other lines, Lines 6 and 7, were 800 m long and were collected transecting the 1200 m lines.

Lines 1–5 consisted of 101 electrodes at 10 m spacing in the centre of the line (200–1000 m) and 20 m spacing along the edges (0–200 and 1000–200 m). Surveys were collected using two line configurations: (1) a roll-along approach where 1200 m long lines are composed of three, 800 m overlapping lines, and (2) a single line approach that utilized the ES10-64C Electrode Selector to increase the electrode capacity and collect along the entire 1200 m line. When available, we use data collected using the roll-along approach. Although this survey configuration has a shorter maximum electrode spacing than the single-line approach with the ES10-64C, the roll-along configuration increases the data density without significantly limiting the depth of investigation recovered by the inversions.

Lines 6 and 7 consisted of 81 electrodes with 10 m spacing in the centre of the line (200–600 m) and 20 m spacing along the line edges (0–200 and 600–800 m). The ES10-64C or roll-along approaches were not required to image these shorter, 800 m-long lines.

3.1.3 Historical vertical electrical sounding field data

Electrical data collected at the Nesjavellir site in 1985 for geothermal resource characterization provide insight into the subsurface electrical properties before geothermal development and wastewater disposal at Nesjavellir (K. Árnason *et al.* 1986a, b). The data were collected using the vertical electrical sounding (VES) method with a Schlumberger array configuration and are detailed in K. Árnason *et al.* (1986b). Four sounding locations were collected within the area of this study, HE-106, HE-109, HE-122 and HE-123 (Fig. 1). The VES method provides a 1-D sounding of the subsurface resistivity and follows a similar methodology as the DC method outlined earlier, where current is injected through two surface electrodes (A and B) and the resulting electrical field is determined by measuring the voltage between another pair of electrodes (M and N). The current electrodes remained fixed around the central sounding location, and the spacing was gradually increased from 4 to 3560 m, with larger spacing probing deeper into the subsurface. The potential electrodes also remain centred around the sounding location, but the electrode spacing remains small (1–200 m) and is increased to preserve the signal-to-noise ratio at large AB spacings.

In the 1-D soundings, near-surface heterogeneities can cause shifts in the apparent resistivity measured at similar AB spacings but with varying MN spacings. Following the method detailed in G.P. Hersir *et al.* (2022), the apparent resistivity measurements at the various MN spacings are corrected by a multiplication factor to minimize misfit to the apparent resistivities measured by the largest MN electrode spacing. The largest MN electrode spacing remains fixed because it is assumed to be least impacted by local heterogeneities. For this data, the multiplication factors range from 0.85 to 1.6. To obtain a 1-D resistivity model, the corrected data were inverted using pyGIMLi software using a smoothness-constrained inversion that minimizes the L2-norm of the data misfit on a logarithmic scale (C. Rücker *et al.* 2017).

3.2 Synthetic cross-hole DCIP

This study also explores the potential of cross-hole DCIP to monitor H_2S mineralization through synthetic experiments. Cross-hole electrical surveying can be advantageous for monitoring deep subsurface processes, improving the spatial resolution of wireline surveying. Monitoring implementations include tracking CO_2 injection systems (C. Schmidt-Hattenberger *et al.* 2011; C.R. Carrigan *et al.* 2013; N. Jia *et al.* 2024), tracer migration (K. Singha & S.M. Gorelick 2005; P.B. Wilkinson *et al.* 2010), and groundwater remediation (T.S. Bording *et al.* 2019; A. Nivorlis *et al.* 2019; L. Lévy *et al.* 2022, 2024a).

The survey design utilizes two boreholes spaced 100 m apart. Each borehole has 31 electrodes, spaced 10 m apart from 150 to 450 m depth. Following a similar approach as L. Lévy *et al.* (2022), the synthetic model is imaged by combining four different acquisition geometries; (1) individual gradient array down the injection borehole, (2) second individual gradient array down the monitoring borehole, (3) AB-MN array configuration with the current dipole (A and B) in the injection borehole and potential dipole (M and N) in the monitoring borehole and (4) AM-BN configuration with the current and potential dipoles split across the two boreholes.

The DCIP starting model for the cross-hole study is constructed by extracting the MPA parameters along NN-4 from the inversion of field data collected in 2020. The time-lapse chargeability changes due to H_2S injection are estimated through reactive transport simulations, where the change in the volume fraction of metallic particles (iron sulfides and iron oxides) is converted to a synthetic chargeability response through eq. (8) (further discussed in Section 3.5).

3.3 Time-lapse DCIP data processing and inversion

The DCIP geophysical modelling and data inversions are performed utilizing a novel electric and electromagnetic geophysical software, EEMverter (G. Fiandaca *et al.* 2023). The data were manually processed by removing outliers in EEMstudio (N.A.L.

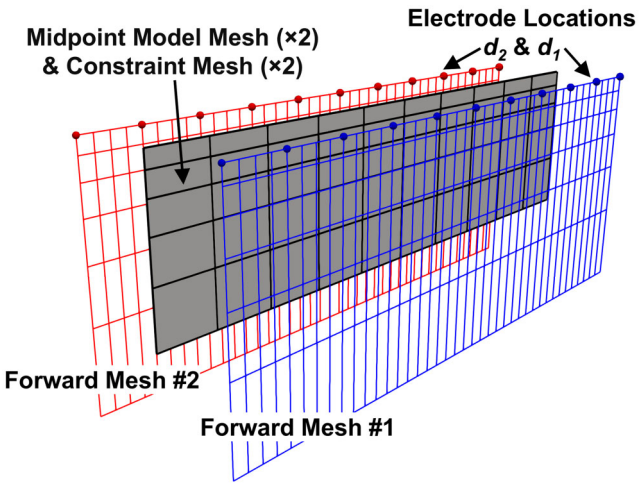

Figure 2. Schematic of the multimesh inversion approach with decoupled forward, constraint and model meshes. The forward meshes are determined based on the electrode locations of the two surveys (spheres). The identical inversion model meshes (midpoint model meshes) and corresponding constraint meshes are calculated from the average electrode positions and are displayed between the forward meshes.

Sullivan *et al.* 2023). Sources of noise can be high contact resistances (∼0.7–1.5 kΩ in our data), polarization of the stainless steel electrodes and capacitive and inductive coupling between cables and the ground. Cultural noise from nearby infrastructure is also a consideration at this field site due to a buried power line and a residential building located within the survey area (Fig. 1). The impact of the surrounding infrastructure on data noise can be observed in the standard deviations mapped in Supporting Information Fig. S1.

EEMverter models the full voltage decay, accounting for the effects of the current waveform and receiver transfer function in the IP forward response (G. Fiandaca *et al.* 2012, 2013). The 2-D DCIP forward response follows the method presented in G. Fiandaca *et al.* (2013) and builds off the 1-D response outlined in G. Fiandaca *et al.* (2012). The time-lapse inversion scheme, as presented in L. Xiao *et al.* (2022), simultaneously inverts two data sets to obtain the corresponding geophysical models. The time-lapse inversion is solved iteratively utilizing the Levenberg–Marquardt adaptive minimization scheme (E. Auken *et al.* 2015; W. Menke 2018). The time-lapse models are constrained through the asymmetric minimum support norm, which penalizes large time-lapse changes to favour the smallest model changes consistent with the data (G. Fiandaca *et al.* 2015b). Minimum support parameter values of $\alpha = 0.01$, $\sigma = 0.1$, $p_1 = 1.35$, $p_2 = 2.0$ were found to minimize both the data and time-lapse model misfits and are used in the inversion of the field DCIP data. Additional details on the forward response time-lapse inversion scheme are included in Supporting Information.

The inversion utilizes a multimesh approach where the model meshes are decoupled from the forward and constraint meshes (Fig. 2) (B. Zhang *et al.* 2021; L. Xiao *et al.* 2022). In the multimesh approach, the values on the inversion model mesh are mapped to the forward mesh utilizing an inverse distance weighting interpolation (L.M. Madsen *et al.* 2020). A separate set of constraint meshes connects the model parameters of individual models, applying horizontal and vertical smoothness, and different models against one another through time-lapse constraints. These constraint meshes share the same geometry as the model mesh and are vertically discretized with a log-increasing spacing. The horizontal discretization of the forward meshes is derived from the electrode placement (x, y and z). It is further subdivided horizontally into four cells to improve the resolution of the forward response without increasing the size of the model space (G. Fiandaca *et al.* 2013). Non-uniform electrode spacing along the survey lines (20 m along the survey edges versus 10 m near the centre) results in mesh cells with variable widths. To avoid numerical artefacts resulting from uneven cell widths, the larger mesh cells (20 m width) were subdivided into two cells of equal widths (10 m).

As the forward meshes are defined by electrode locations, differences in electrode placement between data sets $\mathbf{d}_1$ and $\mathbf{d}_2$ result in misalignment between the meshes. Since the values along each forward mesh are only compared to their respective data set ($\mathbf{d}_1$ or $\mathbf{d}_2$), misalignment between the forward meshes does not pose any issues. However, each of the model and constraint meshes must be spatially aligned to correctly constrain the difference between the models $\mathbf{m}_1$ and $\mathbf{m}_2$. This presents a challenge for time-lapse surveys collected with electrodes that are subject to movement between data sets or that are not permanently installed, such as the data sets collected in this study. To construct two spatially identical model meshes, referred to here as midpoint model meshes, the electrode positions (x, y and z) of data sets $\mathbf{d}_1$ and $\mathbf{d}_2$ are averaged. Each time-lapse inversion model presented in this study is solved on midpoint model meshes to limit the effects of variable electrode placement between the baseline and monitoring data sets ($\mathbf{d}_1$ and $\mathbf{d}_2$).

The effectiveness of the midpoint model mesh approach in managing electrode offset is evaluated through a synthetic test using the resistivity model recovered from the inversion of 2020 field data along Line 4. In this test, the resistivity forward response is simulated along lines with electrodes that are systematically shifted by 2, 4, 6 and 8 m along the line. The resulting offset data are then inverted alongside the unshifted data set using two different inversion approaches: (1) two model meshes that are offset based on the electrode placement of each line and (2) two identical midpoint model meshes (Fig. 2). Since the data sets are generated from the same resistivity model and noise is not added in this synthetic test, time-lapse variability is related to electrode offset.

The depth of investigation (DOI) is determined using a cumulated approximate analysis approach (G. Fiandaca *et al.* 2015a; P.K. Maurya *et al.* 2018). In this method, the sensitivities at each model layer, defined by the Jacobian matrix elements and covariance matrix, are summed upwards for each column of the model matrix. This provides a sensitivity value for each layer, expressing the cumulative sensitivity of the inversion from that layer to the deepest layer. A threshold sensitivity value, selected here as 5.0 (G. Fiandaca *et al.* 2015a; P.K. Maurya *et al.* 2018), defines the DOI, below which each of the recovered model parameters is no longer data-driven.

3.4 Geochemical analysis

The reactive transport models are parametrized with geochemical data collected from groundwater, injection water and basalt cuttings sampled at the Nesjavellir site. Groundwater samples were collected throughout the area in 1991, 2007 and 2008 (B. Sigfusson *et al.* 2011), and at the NL-12 borehole in November

2021 (D.A. Ciraula *et al.* 2024). Injection water samples were collected at the injection boreholes in November 2021 (D.A. Ciraula *et al.* 2024). The groundwater and injection water compositions were constrained through Ion Chromatography (IC) and inductively coupled plasma optical emission spectroscopy (ICP-OES) analysis (D.A. Ciraula *et al.* 2024). Additionally, H_2S concentrations were measured via mercury acetate titration (S. Arnórsson *et al.* 2006), and CO_2 concentrations were measured through modified alkalinity titration using 0.1 M HCl and 0.1 M NaOH (G.H. Jeffery *et al.* 1989; A. Stefánsson *et al.* 2007).

The rock composition was determined from borehole cuttings from injection wells NN-3, NN-4 and NN-7, and whole-rock composition of the basalt was constrained through ICP-OES analysis (D.A. Ciraula *et al.* 2024). The primary minerals in the basaltic host rock were estimated using a linear regression approach, which determined the relative mineral proportions based on the mineral compositions and the measured oxide weight percentages of the whole rock (D.A. Ciraula 2025; D.A. Ciraula *et al.*, in preparation). Further details on the chemical methods and the fluid and rock composition utilized in the reactive transport models can be found in D.A. Ciraula *et al.* (2024).

3.5 Integrating DCIP with reactive transport modelling

3.5.1 Principles of reactive transport

Reactive transport simulators couple chemical reactions with fluid and heat transport (C.I. Steefel & A.C. Lasaga 1994; C.I. Steefel *et al.* 2005; S. Molins & P. Knabner 2019). Simulations solve the advection-dispersion equation, a partial differential equation that satisfies the conservation of mass and momentum, considering advective fluid flow, dispersion processes (molecular diffusion and mechanical dispersion), fluid sources and sinks and chemical reactions (e.g. J. Carrera *et al.* 2022). Through this coupled simulation, reactive transport predicts how geochemical and hydrological systems evolve over space and time, enabling a better understanding of the subsurface processes that control these changes. The reactive transport simulation outputs of particular relevance in this study are the mineral abundances. Further details on reactive transport modelling are beyond the scope of this paper; readers are referred to C.I. Steefel *et al.* (2005) and J. Carrera *et al.* (2022) for additional background on the methodology, and to E.S. Aradóttir *et al.* (2012) and D.A. Ciraula (2025) for reactive transport modelling of mineral storage approaches in Iceland.

3.5.2 3-D Reactive transport integration with surface DCIP

In this study, reactive transport models predict the degree of H_2S mineralization to (1) guide interpretation of the geophysical inversion models, (2) evaluate the sensitivity of the DCIP monitoring to H_2S mineralization and (3) constrain the underlying processes controlling H_2S mineralization and impacting the IP response. A full description of the reactive transport model is presented in D.A. Ciraula (2025) and D.A. Ciraula *et al.* (in preparation), but a brief description is included here to provide context for the integration with DCIP. The reactive transport models are constructed in TOUGHREACT (T. Xu *et al.* 2011) using calibrated flow and chemical parameters based on borehole temperature, tracer and water chemistry measurements prior to integration with the DCIP geophysical surveying. The development and calibration of the reactive transport model are done independently of geophysical field data to ensure that the simulations serve as an independent method for interpreting the geophysical responses. The model is constructed using a 3-D, multiple interacting continua (MINC) framework (K. Pruess & T.N. Narasimhan 1985), considering non-isothermal fluid flow.

The reactive transport model simulates surface disposal of the geothermal wastewater, pumping of shallow freshwater wells and the injection of H_2S-rich water into the shallow groundwater system. The Nesjavellir operator, Reykjavik Energy, provided the injection rates and water temperature. Shallow well pumping rates, surface wastewater disposal rates and wastewater temperatures are estimated from values in E. Gómez-Díaz *et al.* (2022). The geological model considers variable host rock geology, featuring a sequence of hyaloclastite and lava flow lithologic units. The geology builds on the model presented in E. Gómez-Díaz *et al.* (2022), and was constructed using surface geological maps, borehole cuttings (H.M. Helgadóttir 2021; D.A. Ciraula *et al.* 2024) and borehole data from internal reports of the Nesjavellir operator, Reykjavik Energy (Supporting Information Fig. S2). The hyaloclastites are characterized by larger porosity and permeability values than the lava flows (Supporting Information Table S1), and contain more abundant basaltic glass, as observed in typical Icelandic basalts (e.g. S.W. Scott *et al.* 2023).

The primary minerals considered in the study consist of plagioclase, pyroxenes, olivine, iron oxides (magnetite and ilmenite) and basaltic glass. Alteration minerals available to precipitate include zeolites, carbonates, smectite clays, iron oxide (goethite), iron sulfides (pyrite and pyrrhotite), amorphous silica and elemental sulfur. Dissolution and precipitation of primary and alteration minerals are kinetically controlled. They are modelled based on transition state theory, which considers the phase's rate constant, reactive surface area, saturation conditions considering the thermodynamic conditions and additional acid- and base-catalysed mechanisms (e.g. J.L. Palandri & Y.K. Kharaka 2004; T. Xu *et al.* 2011). A complete list of the primary and alteration minerals, along with their kinetic rate parameters, is included in Supporting Information Tables S2 and S3. The thermodynamic constants are provided in the *carbfix.dat* thermodynamic data base (M. Voigt *et al.* 2018) with redox conditions determined by the HS^-/SO_4^{2-} couple. The reactive surface areas of each mineral, a value often uncertain in reactive transport models, were calibrated by simulating 250 yr of ambient groundwater reactive transport and ensuring a match to groundwater fluid compositions.

To integrate the reactive transport model with the DCIP inversion results, we calculate IP chargeability changes from the simulated iron sulfide precipitation and iron oxide dissolution using eq. (8). We simulate H_2S injection for two durations: 6 months to compare with the field geophysical data and 25 yr to evaluate the long-term changes in the geophysical response. The chargeability changes are then added to the 2020 baseline DCIP models to construct predicted 2021 models along the survey lines.

3.5.3 2-D Radial reactive transport integration with cross-hole DCIP

Reactive transport modelling also produces synthetic geophysical responses to evaluate cross-hole DCIP as a monitoring method for H_2S mineral storage. For the cross-hole synthetic modelling, a 2-D radial reactive transport model is developed

in TOUGHREACT (T. Xu *et al.* 2011) with the same geochemical parameterization as the 3-D model. The 2-D model has cells refined to 5×5 m around the injection borehole (Supporting Information Fig. S3) to enhance the simulation's resolution of the near-borehole processes that the cross-hole DCIP seeks to image. The refined radial geometry captures the flow and transport near the injection boreholes while ensuring computational efficiency. Two separate long-term (25 yr) simulations of H_2S injection are performed using different injection fluids: (1) the H_2S-rich water measured at the NN-4 wellhead and (2) a higher concentration H_2S-rich water that is injected into the deeper NJ-18 borehole (2136 m deep) at Nesjavellir (I.M. Galeczka *et al.* 2022). We simulate both scenarios to gain insight into the implementation of cross-hole monitoring of deep H_2S injection. The NJ-18 injection well receives wastewater from the 'Carbfix' emission reduction method, which uses scrubbing towers to increase the concentration of H_2S and CO_2 dissolved into the injection water. At Nesjavellir, these higher concentration fluids are designated for deeper injection, where the risk for surface water contamination is reduced. For an overview of the Carbfix method and its implementation at Nesjavellir, readers are referred to the work by J.M. Matter *et al.* (2016) and I.M. Galeczka *et al.* (2022).

Similar to the integration of the 3-D reactive transport model and surface DCIP, the change in volume fraction of metallic particles (iron sulfides and iron oxides) calculated through the 2-D radial reactive transport simulations is used in eq. (8) to generate synthetic chargeability response changes. Random Gaussian noise is added to the synthetic DC voltages and the polarization curves with a standard deviation of 2 per cent of the data values to better represent field conditions.

4 RESULTS

4.1 Reactive transport modelling

The results of the reactive transport model are first detailed to provide relevant context for the interpretation of the geophysics and the joint geochemical–geophysical integration. Relevant to the IP response in this study, the model indicates that iron released upon the alteration, primarily from basaltic glass and iron-bearing olivine, results in pyrite formation. H_2S mineralization is effective, with roughly 70 per cent of the injected H_2S anticipated to mineralize as pyrite within the first year of injection, and 87 per cent over 25 yr of continuous injection. Based on the injection fluid compositions, the average injection rates and a mineralization rate of 87 per cent, we estimate that 284 m^3 of pyrite forms each year. However, the reactive transport simulations show that the high-permeability fractured basalt effectively transports the H_2S-rich fluid from the injection wells, leading to pyrite mineralization distributed throughout the subsurface. This distribution, along with the limited total mass of injected H_2S, yields minute pyrite volume fractions observed after the first six months of injection ($< 1 \times 10^{-4}$ per cent of the porous media volume within 75 m of the injection well).

In addition to pyrite formation, alteration minerals include zeolites, smectite clays, carbonates, amorphous silica and minor Fe(III)-oxides. These alteration products are consistent with the mineralogical changes expected during the alteration of Icelandic basalts in warm water (e.g. S.W. Scott *et al.* 2023). Within the basalt (hyaloclastite) rock matrix, zeolites and smectite clays comprise the majority of the alteration minerals after six months of injection, approaching $\sim 5 \times 10^{-4}$ per cent and $\sim 1 \times 10^{-3}$ per cent of total volume within 75 m of the injection well, respectively. Given the small volumes of alteration products, absolute changes in the rock porosity and permeability over long-term injection (25 yr) are low ($\phi_{25} - \phi_0 = -0.06$ per cent, $\kappa_{25}/\kappa_0 = 0.75$ per cent). Additional reactive transport model results that extend beyond the scope of this paper can be found in D.A. Ciraula (2025) and D.A. Ciraula *et al.* (in preparation).

4.2 Validating midpoint model mesh

The time-lapse inversions utilizing the shared midpoint model mesh are found to reduce erroneous time-lapse changes due to electrode misplacement in synthetic data as compared to inversions where the individual model meshes are offset (Fig. 3). This is essential for this study as the field campaigns were carried out a year apart, and the H_2S injection site did not offer the opportunity to install electrodes permanently. Given a 4 m shift in the electrode placement, the midpoint model mesh approach recovers an average absolute change (i.e. $\bar{x} = \frac{1}{n}\sum_{i=1}^{n}\left|\frac{m_{2,i}-m_{1,i}}{m_{1,i}} \times 100\right|$) of 0.1 per cent compared to 2.1 per cent for the offset mesh approach. The midpoint model mesh approach also recovers better inversion misfit than the offset model mesh approach: time-lapse misfit norm = 0.3 versus 2.1, first data set L2 norm misfit = 1.2 versus 3.6, second data set L2 norm misfit = 1.4 versus 3.9. Similar misfits are observed for the other offsets.

4.3 Integrating surface DCIP and reactive transport modelling

4.3.1 1985 versus 2020 resistivity to validate reactive transport parameters

Changes between the resistivity model from 2020 DCIP lines and the 1985 VES model are compared to subsurface changes predicted by the reactive transport modelling. Between 1985 and 2020, resistivities decreased in the shallow groundwater system, as can be seen at the location of soundings HE-109 and HE-123, in the elevation range 0–100 m above sea level (m.a.s.l.) (Fig. 4). Within this depth interval, the 2020 model recovers an average resistivity of ∼325 Ωm compared to an average resistivity of 1925 Ωm in the 1985 model. These soundings are located northeast of the injection boreholes, along the primary direction of groundwater flow. Soundings HE-122 and HE-106, located southeast of the injection wells away from the main groundwater flow direction, do not exhibit the same resistivity decreases and capture similar resistivity trends as the 2020 models. Here, we utilize the reactive transport model to provide a comprehensive understanding of the factors contributing to the resistivity decrease.

Variations in the total resistivity reflect changes happening in three parallel conduction pathways: electrolytic conduction, surface conduction in the electrical-double layer at the fluid-grain interface and intra-solid conduction paths within the smectite clay sheets (e.g. M. Wyllie & P. Southwick 1954; J.G. McKelvey *et al.* 1955; M.H. Waxman & L.J. Smits 1968; L. Lévy *et al.* 2018).

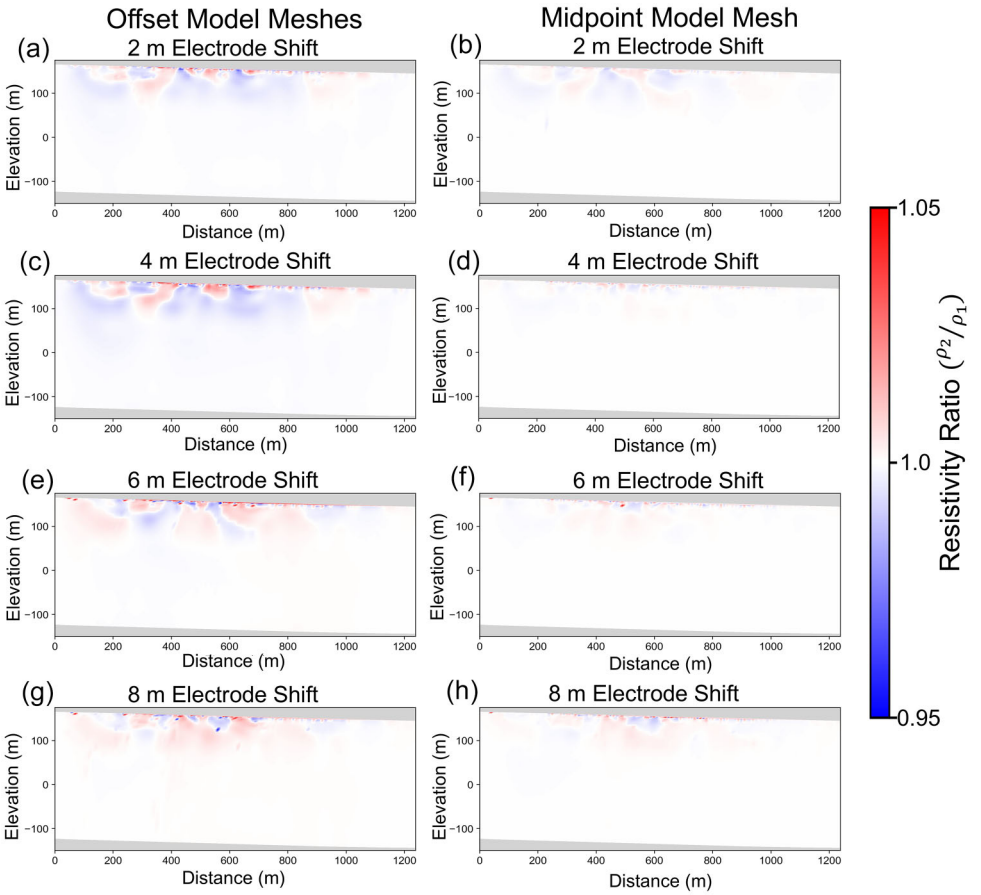

Figure 3. Time-lapse inversion results obtained using model meshes offset from one another (left column) and identical, midpoint model meshes (right column). The magnitude of the electrode misplacement (shift) is shown from a range of 2–8 m.

This is expressed by eq. (9) (L. Lévy *et al.* 2018),

$$\frac{1}{\rho_{\text{tot}}} = \sigma_{\text{tot}} = \frac{\sigma_w}{F} + \sigma_s + \frac{\frac{\sigma_w}{F'}}{1 + \frac{\sigma_w}{F' X_{\text{smect}} \sigma_{\text{smect}}}}, \tag{9}$$

where σ_w is the fluid conductivity (S m^{-1}), σ_s is the surface conductivity pathway (S m^{-1}), F is the formation factor from Archie's Law (G.E. Archie 1942) that depends on the porosity (ϕ) and the cementation factor (m) of the rock ($F = \phi^{-m}$), F' is the formation factor of the intrasolid conduction pathway, X_{smect} is the volume fraction of smectite in the bulk rock and σ_{smect} is the intrinsic conduction of the solid smectite (S m^{-1}).

The measured resistivity in 1985 is expected to be controlled by electrolytic and surface conduction because smectite clays are not identified in the shallow unaltered basalts at these depths prior to geothermal wastewater injection (H.M. Helgadóttir 2021; D.A. Ciraula *et al.* 2024). The reactive transport model considers changes to the fluid chemistry and temperature (R.B. McCleskey *et al.* 2012) and predicts a fluid conductivity increase from 0.009 to 0.034 S m^{-1} in 2020 near the 1985 sounding locations. These fluid conductivities align with field measurements of fresh groundwater ($6 \times 10^{-3}\ \text{S m}^{-1}$) and groundwater mixed with geothermal wastewater (0.037–0.046 S m^{-1}) observed in NL-12 between 2001 and 2021. To determine the impact of the warm, conductive geothermal wastewater on the total resistivity, we first solve for the surface conductivity term using the field resistivity measured in 1985 ($\rho_{\text{field},1985} = 1925\ \Omega\text{m}$), $\sigma_{\text{freshwater}} = 6 \times 10^{-3}\ \text{S m}^{-1}$ (S. Zarandi & G. Ivarsson 2010; G. Ívarsson 2019), $\phi = 25$ per cent (V. Stefánsson 1991; A.Q.M. noz 1996), and $m = 2.06$, indicative of minimally altered basalts (alteration < 10 wt. per cent) from L. Lévy *et al.* (2018) and similar to values observed in A. Revil *et al.* (2017a). We identify a surface conductivity of $2 \times 10^{-4}\ \text{S m}^{-1}$, similar to laboratory values recovered for minimally altered basalts in L. Lévy *et al.* (2018). Substituting the fresh water conductivity with the more conductive 2020 fluids ($4 \times 10^{-2}\ \text{S m}^{-1}$) in eq. (9), we find the total resistivity decreases from 1925 to 400 Ωm, constituting most of the measured resistivity change.

While the majority of the resistivity decrease from 1985 to 2020 can be attributed to the presence of warm, conductive geothermal wastewater in the shallow groundwater system, smectite clay mineralization upon basalt alteration may also contribute to decreasing the resistivity (e.g. L. Lévy *et al.* 2018). The reactive transport model predicts the precipitation of smectite, with final volume fractions in the range 0.02–0.15 per cent in the region of the field resistivity decrease. Using average values from basalt samples containing smectite measured in L. Lévy *et al.* (2018), we assign $F' = 29.1$ and $\sigma_{\text{smect}} = 0.65\ \text{S m}^{-1}$ in the intrasolid conduction term contained in eq. (9). This range of predicted smectite abundance further decreases the estimated 2020 resistivity from 400 to 330–385 Ωm. These values are similar to the resistivities observed in 2020 ($\rho_{\text{field},2020} = 325\ \Omega\text{m}$), and provide a process-based explanation for the field changes measured using geophysics.

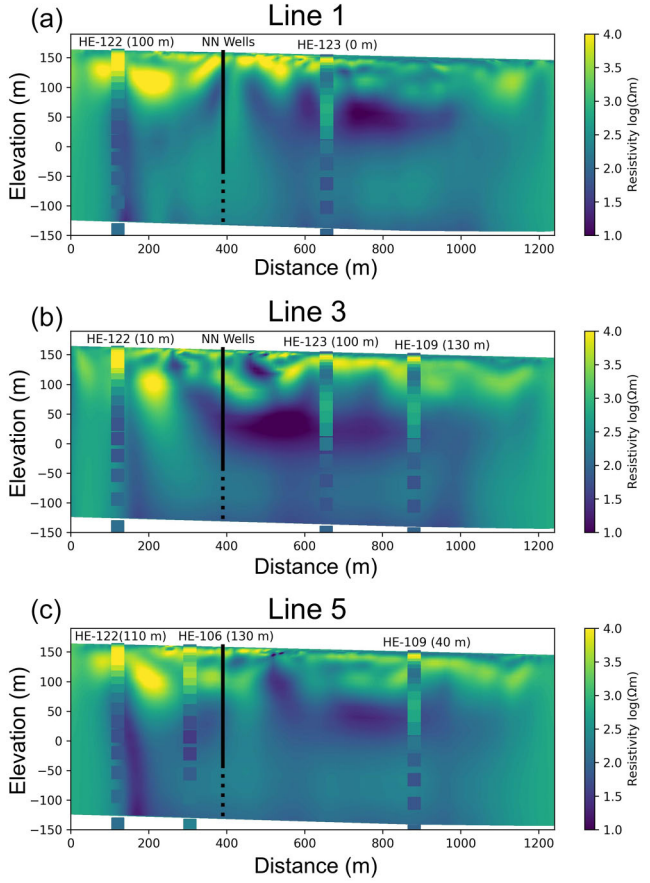

Figure 4. Results of the VES inversions of the 1985 data (HE-106, HE-109, HE-122, HE-123) plotted over the 2020 DC resistivity model for Lines 1, 3 and 5. The distance from the sounding to the line is included with the sounding labels. The black lines indicate the location of the NN injection wells, with the solid and dashed segments representing the cased and open intervals, respectively.

To further explore how the resistivity measurements can validate the reactive transport model, we utilize a relationship established in L. Lévy *et al.* (2020) between the electrical conductivity, smectite volume fraction (θ_{smectite}) and permeability (k) at low ($< 0.5\,\text{S}\,\text{m}^{-1}$), uniform fluid conductivity, following:

$$\frac{1}{\rho} = \sigma = \frac{B\,\theta_{\text{smectite}}}{a\,k^{-\beta}}. \tag{10}$$

In this empirical relationship, the denominator defines a formation factor [i.e. how much the rock matrix impedes electrical current, G.E. Archie (1942)] and the constants have values a= 14.4, B= 8.4 $\text{S}\,\text{m}^{-1}$ and β = 0.25. This relationship does not inform changes observed in the field resistivity from 1985 to 2020, but provides a means to assess the permeability values used in the reactive transport model using the average smectite abundance predicted by the reactive transport model in 2020 (0.06 per cent) and the resistivity values measured in 2020 (325 Ωm). We find that a high permeability value of 7.9 $\times 10^{-12}$ m^2 is required to capture the resistivity decrease observed in this alteration zone. This permeability is consistent with the x- and y-permeabilities assigned to the fractured hyaloclastite in the reactive transport model (1.0 $\times 10^{-12}$ m^2 and 9.7 $\times 10^{-11}$ m^2, respectively), which were calibrated to temperature logs in nearby monitoring boreholes (D.A. Ciraula 2025; D.A. Ciraula *et al.*, in preparation). Furthermore, these values align with values expected for permeable basalts (R.A. Freeze & J.A. Cherry 1979), and with the upper limit of values observed in unaltered, Icelandic hyaloclastites (S.W. Scott *et al.* 2023).

Overall, this integration establishes a framework in which electrical resistivity geophysical surveys can validate field-scale reactive transport models. While the integration presented here serves only to support for the general fluid conductivity changes, smectite mineralization and high permeabilities of the present model, future studies with better resolution of the time-lapse geophysics could utilize these relationships between resistivity, fluid conductivity, smectite content and permeability, alongside field samples quantifying fluid chemistry, smectite abundance and permeability, to explore high-resolution calibration of reactive transport parameters (chemical and physical) to resistivity data.

4.3.2 *Synthetic IP from reactive transport*

The expected change in chargeability due to H_2S injection between the baseline and monitoring DCIP surveys is predicted by the reactive transport model along each of the DCIP survey lines and is shown in Fig. 5. The chargeability changes extend beyond the injection wells to larger distances along the lines, reflecting the regional groundwater flow direction towards Lake Thingvellir (from southwest to northeast). The changes are expected to be very small, at less than 0.02 $\text{mV}\,\text{V}^{-1}$ during the six months of injection. Additionally, the changes are limited to depths greater than 280 m (elevation = −120 m.a.s.l.) due to the 200 m of borehole casing. The largest increase in volume fraction of metallic particles and chargeability values is closest to the NN-4 injection borehole along Line 4, as NN-4 had one of the highest injection rates of H_2S charged water over the survey period at 105 $\text{kg}\,\text{s}^{-1}$ (total) compared to 11–43 $\text{kg}\,\text{s}^{-1}$ at the other injection wells. Along Line 4, deep chargeability changes are observed as a result of injection into NN-3. However, injection rates average only 15 $\text{kg}\,\text{s}^{-1}$ into NN-3, resulting in chargeability changes with smaller magnitudes (0.005 $\text{mV}\,\text{V}^{-1}$) at depths greater than 360 m (elevation = −200 m.a.s.l.).

Injection into NN-4 also produces chargeability changes along Line 3, but the changes occur further along the line as the fluid laterally migrates from the NN-4 feed zones. Changes along Line 5 result from fluid injection near the power plant, with small contributions at a distance of 400 m along the line from H_2S injection through the NN-5 and NN-6 boreholes, located 80 m southeast of the line. Minimal changes are seen along Lines 1 and 2, as the nearby NN-7 injection borehole is deviated away from these lines.

The expected chargeability changes are also calculated for long-term injection (25 yr) of H_2S at Nesjavellir (Supporting Information Fig. S4). After 25 yr of injection, the expected chargeability anomaly remains small, at less than 0.5 $\text{mV}\,\text{V}^{-1}$ along Line 4.

4.4 Time-lapse inversions of 2020-2021 field data

The time-lapse inversions recovered a sufficient fit to the data, with an average DC L2-norm misfit (δd_{DC}) of $\delta d_{\text{DC,2020}}$ =3.4,

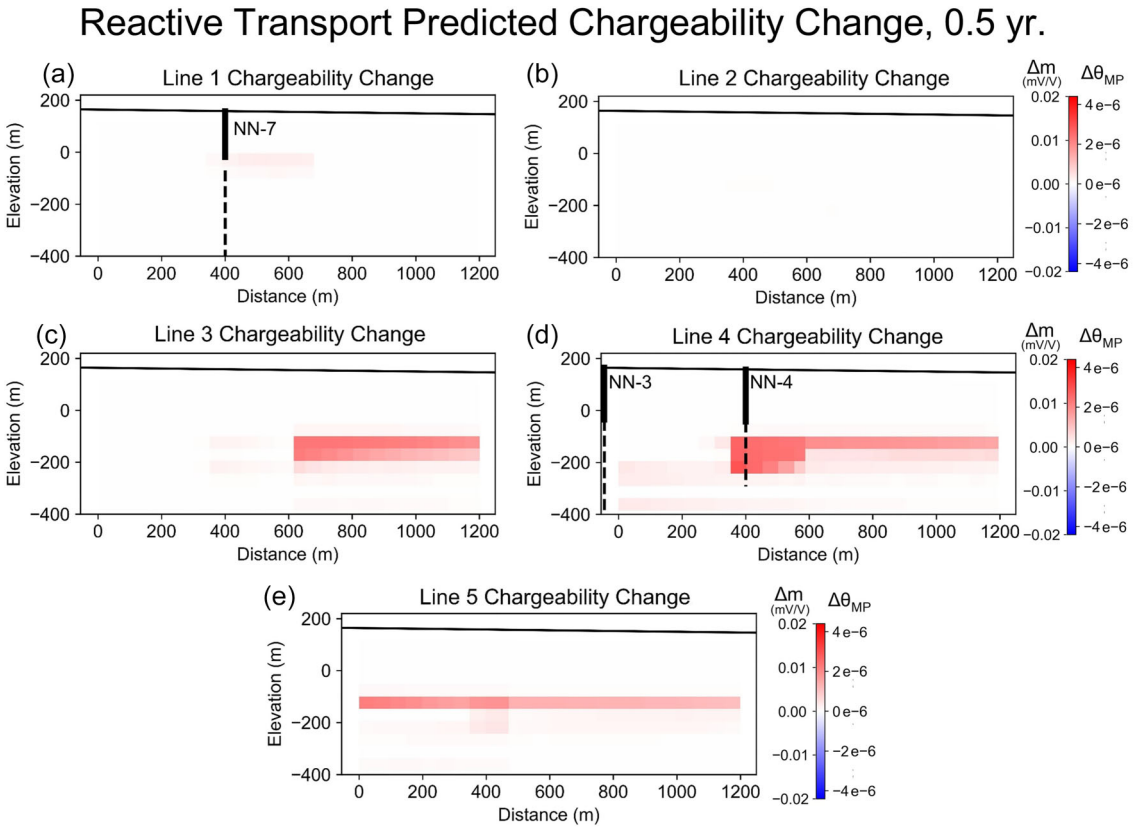

Figure 5. Results of the reactive transport model extracted along the field DCIP survey lines showing the minute expected change in metallic particles ($\Delta\theta_{MP}$= iron sulfides and iron oxides) and the corresponding chargeability change (Δm) following six months of H_2S injection. The NN-3, NN-4 and NN-7 injection wells that intersect the survey lines are displayed as black lines (solid = casing, dashed = open interval).

$\delta d_{DC,2021}$ =3.6 and an average IP L2-norm misfit (δd_{IP}) of $\delta d_{IP,2020}$ =2.0, $\delta d_{IP,2021}$ =1.5. The largest data misfits are observed near infrastructure, such as the buried power line, the house and the injection boreholes/hot water pipes.

The results of the time-lapse IP inversions are shown in Fig. 6 as the change in the chargeability and the equivalent change in volume fraction of metallic particles (iron sulfides and iron oxides). The results are trimmed to the DOI and at the water table (elevation = 110 m.a.s.l.) to focus on changes occurring within the fully saturated subsurface. The DC inversion resolves down to 200–250 m depth (elevation = ∼0 to −100 m.a.s.l.). However, the centre of Line 3, which is next to the house, only images to ∼100 m depth. The IP DOI reaches 100 m depth (elevation = ∼50 m.a.s.l.) along the southern extent of the survey and 150 m depth (elevation = ∼0 m.a.s.l.) towards the northern extent of the survey. Similar to the decreased DC DOI at the centre of Line 3, the IP DOI at the centre of Lines 2–5 near the house and injection infrastructure falls above the water table, limiting the IP data within 100 m of the house. Overall, the DOI values are roughly 50 m deeper along the northern extent of the line (away from the injection wells) compared to the southern extent (near the injection wells) for both the DC and IP inversions.

The time-lapse inversions reveal little change between the 2020 and 2021 DC and IP models. Aside from a few isolated nodes, changes in the chargeability and resistivity are negligible (Fig. 6, Supporting Information Fig. S5). The large range

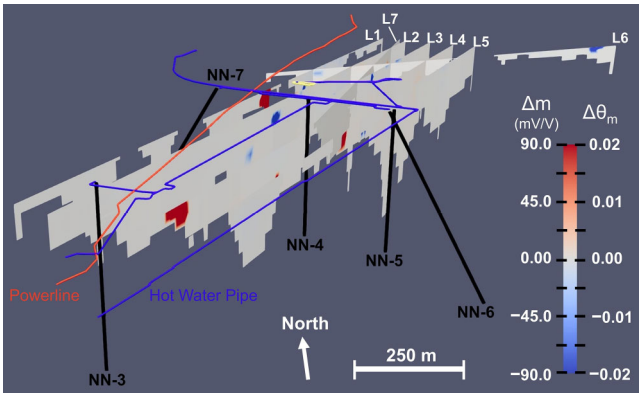

Figure 6. Results of the time-lapse IP inversion recovering changes in chargeability (m) and volume fraction of metallic particles (θ_m) following six months of H_2S injection. The casings of the NN injection wells (∼200 m depth) are displayed as vertical lines and indicate the minimum depth that H_2S-charged water enters the subsurface. Beneath the casing, the wells are open and extend another 200–350 m. The results are trimmed to the water table at ∼110 m depth and to the depth of investigation. Infrastructure in the survey area is displayed along the ground surface (yellow outline = house, blue line = hot water/steam pipes, red line = buried power line).

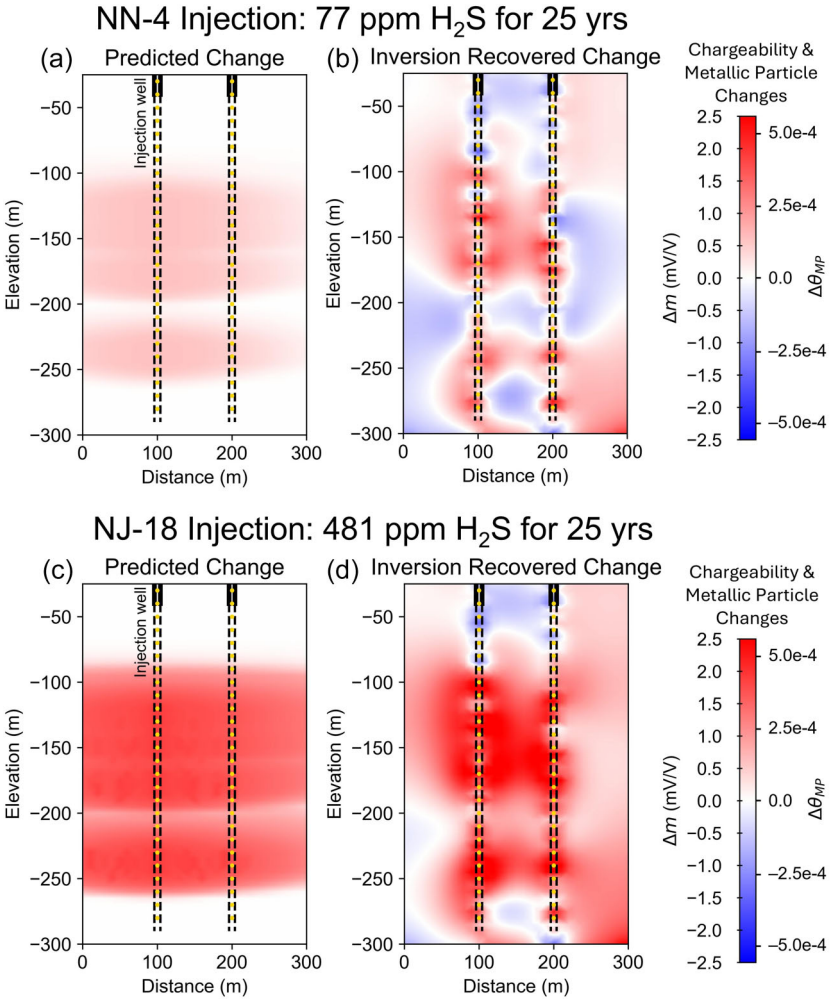

Figure 7. Results of the synthetic cross-hole modelling showing expected chargeability (m) change and the corresponding change in volume fraction of metallic particles (θ_{MP}) following 25 yr of injection into NN-4 (top row) and NJ-18 (bottom row). The NN-4 and NJ-18 injection fluids have H_2S concentrations of 77 ppm (D.A. Ciraula *et al.* 2024) and 481 ppm (I.M. Galeczka *et al.* 2022), respectively. The right plots show the time-lapse inversion results of the predicted synthetic data with 2 per cent Gaussian noise added to the IP decays and the DC voltages. Solid lines indicate borehole casing, dashed lines indicate the open boreholes and yellow dots within the boreholes indicate the electrode locations.

of chargeability magnitude plotted on the colourscale of Fig. 6 compared to the chargeability change expected from the reactive transport model (Fig. 5) highlights the magnitude of the noise in the surface DCIP field data relative to the predicted signal. This resolution limitation is further discussed Section 5.2.2. The large (>450 mV V^{-1}) isolated chargeability change at the southern extent of Line 4 aligns with the intersection of the buried power line. Similarly, the large changes observed along Line 3, beyond the residential building, align with areas of large data misfit and are near the DOI. Most DC resistivity changes are also isolated near infrastructure, aside from a broad increase in the DC resistivity along Line 5 near the NN-5 injection borehole (Supporting Information Fig. S5). However, the 2021 Line 5 data is notably noisy (Supporting Information Fig. S1) and the inversion misfit is large compared to the other lines (6.1 versus 3–4), suggesting that this increase could be due to noise, such as coupling. Interestingly, the average injection rate of warm wastewater into NN-5 in the six months leading up to the 2020 survey was 62 L s^{-1}, compared to 38 L s^{-1} preceding the 2021 survey, which could also contribute to the increase in resistivity. Overall, the time-lapse inversions show agreement with the results of the reactive transport models and do not indicate systematic increases or decreases in chargeability or resistivity due to H_2S injection.

4.5 Integrating cross-hole DCIP and reactive transport modelling

Similar to the integration with surface DCIP, reactive transport modelling is integrated with cross-hole DCIP to evaluate the method's sensitivity to expected response changes. In the 5 × 5 m cells within the near-borehole environment, the radial reactive transport model predicts minor chargeability increases of 0.6 and 1.9 mV V^{-1} after 25 yr of injection of the NN-4 and NJ-18 H_2S-charged waters, respectively [Figs 7(a)/(c)]. These chargeability increases coincide with the NN-4 feed zones at −120, −140, −170 and −228 m above sea level.

The time-lapse inversion results for the synthetic data sets from 25 yr of H_2S injection with 2 per cent Gaussian noise added are shown in Figs 7(b) and (d). For the NN-4 injection fluid, chargeability increases at the depth intervals are partially

recovered within 25 m of the boreholes. However, the spatial resolution is severely impacted by the background noise. Moreover, chargeability decreases of equivalent magnitude to the predicted increase (i.e. -0.5 mV V^{-1}) are introduced due to the background noise, making the interpretation of pyrite mineralization highly uncertain. Compared to NN-4, the larger predicted anomaly from the injection of NJ-18 fluids is better recovered. The inversion reconstructs the magnitude and spatial extent of the changes within 25–75 m from the boreholes, and extends the full 100 m between the boreholes near the feed zones. Beyond 75 m from the boreholes, the inversion resolution diminishes and the background noise dominates the response changes.

The ability of cross-hole DCIP to resolve chargeability changes from shorter injection durations is also tested through time-lapse inversions of synthetic data from 5 yr of H_2S injection (Supporting Information Fig. S6). The inversion does not recover the minimal expected chargeability changes (0.15 mV V^{-1}) from the injection of NN-4 fluids. The chargeability changes from five years of H_2S injection into NJ-18 (0.5 mV V^{-1}) are slightly better resolved compared to NN-4 due to larger anomalies from the highly concentrated H_2S injection fluids. However, the changes are limited to 10–20 m from the boreholes, and the data noise reduces the vertical resolution down the borehole.

5 DISCUSSION

5.1 Reducing artefacts from variable electrode placement

The synthetic modelling of the flexible inversion grid approach presented here improves the resolution of time-lapse inversions. The mid-point model mesh approach, constructed considering the average location among the electrodes, represents a simple yet effective approach to minimize artefacts introduced by variable electrode placement between time-lapse electrical surveys. Ultimately, this promotes higher resolution time-lapse imaging and allows for more flexible field implementation of time-lapse electrical surveys. Furthermore, this method could be applied alongside other approaches that further decrease artefacts, such as implementing array configurations that are less sensitive to variable electrode placement (B. Zhou & T. Dahlin 2003), correcting electrode location based on changes in apparent resistivity (P.B. Wilkinson *et al.* 2010, 2015), and simultaneously inverting for electrode displacement and geoelectrical parameters (J.H. Kim *et al.* 2014; M.H. Loke *et al.* 2018).

5.2 DCIP monitoring of H_2S mineral storage at Nesjavellir

5.2.1 Joint interpretation of reactive transport and field DCIP

In agreement with previous laboratory (C. Marieni *et al.* 2018; J. Prikryl *et al.* 2018) and field studies (I. Gunnarsson *et al.* 2018; D.E. Clark *et al.* 2020), the reactive transport model recovers effective H_2S mineralization with 70 per cent of the total injected H_2S mineralizing during the first year of H_2S injection. However, the expected geophysical response from the H_2S mineralization resulting from the current injection system at Nesjavellir is minimal, suggesting that it cannot be detected with surface DCIP. The results of the time-lapse IP collected at the Nesjavellir injection site confirm these findings, as the method does not recover changes indicative of H_2S mineralization following six months of H_2S injection. The few observed changes are large and isolated, with metallic particle volume fractions > 10 per cent, far greater than the maximum volume changes of iron sulfides and iron oxides predicted by the reactive transport model. Thanks to the joint interpretation of the time-lapse IP changes with the reactive transport model, the infrastructure effects on the data can be distinguished from the mineralogical changes.

In this study, the reactive transport is used *a-poseriori* to interpret the results of field data. Such integrated approaches could be used *a-priori* in future studies to optimize survey design and evaluate the method's sensitivity to the subsurface processes of interest. This idea is explored further in the integration with cross-hole DCIP monitoring, discussed in the following section.

5.2.2 Surface DCIP detection limit analysis

To assess the resolution of the surface DCIP survey to H_2S mineralization in a more quantitative manner, we calculate SNRs resulting from various degrees of pyrite mineralization at different depths throughout the model. The SNRs are calculated utilizing the inversion sensitivity (Jacobian) matrix ($J_{i,j}$), the data standard deviation σ_i, the inversion model chargeability (m_j) and chargeability changes (Δm_j) in eq. (11).

$$\mathrm{SNR}_i = \frac{J_{i,j}}{\sigma_i} \cdot \frac{\Delta m_j}{m_j} = \frac{\Delta d_i(_{\Delta m_j})}{\sigma_i}\,, \tag{11}$$

where the Jacobian is computed in the logarithmic parameter space (i.e. $J_{i,j} = \frac{\partial d_i}{\partial \log(m_j)}$) and $\Delta d_i(_{\Delta m_j})$ is the data variation due to the model variation. The SNR vector is defined for each time gate of the IP decay curve, and the root mean square is calculated across the individual decay curves to provide a single amplitude value for each quadrapole. SNR values greater than one indicate that the chargeability signal, which is attributed only to pyrite mineralization in this analysis, is greater than the noise.

The analysis shows a clear decrease in the SNR with decreasing pyrite volume and increasing pyrite depth (Fig. 8). The surface DCIP lacks resolution for bodies of pyrite with volume percentages ≤ 1 per cent at depths greater than 100 m. Smaller anomalies comprising 0.1 vol. per cent pyrite does not produce a surface DCIP signal magnitude greater than the noise at any depth. For larger anomalies comprising 10 vol. per cent pyrite, the SNR slightly exceeds one for the mid-depth anomaly from 100–200 m depth (elevation -50–50 m.a.s.l.) and greatly exceeds one for shallow anomaly depths from 50 to 150 m depth (elevation 25–125 m.a.s.l.). The surface DCIP data struggles to resolve signals greater than the noise for all pyrite anomalies at the deep injection depth (> 200 m depth, elevation < -50 m.a.s.l.).

These results quantitatively demonstrate the surface DCIP method's lack of resolution of the minute pyrite abundances ($< 4 \times 10^{-4}$ per cent) predicted by the reactive transport model over the six months of H_2S injection. The analysis supports the interpretation that the lack of change in the time-lapse DCIP survey does not directly indicate unsuccessful H_2S mineralization, but rather could indicate insignificant signal change, as suggested by the reactive transport model. Based on the resolution of the surface DCIP from the detection limit analysis and the rate of pyrite mineralization at the Nesjavellir injection site from the reactive transport simulations, monitoring long-term injection with surface DCIP remains unfeasible.

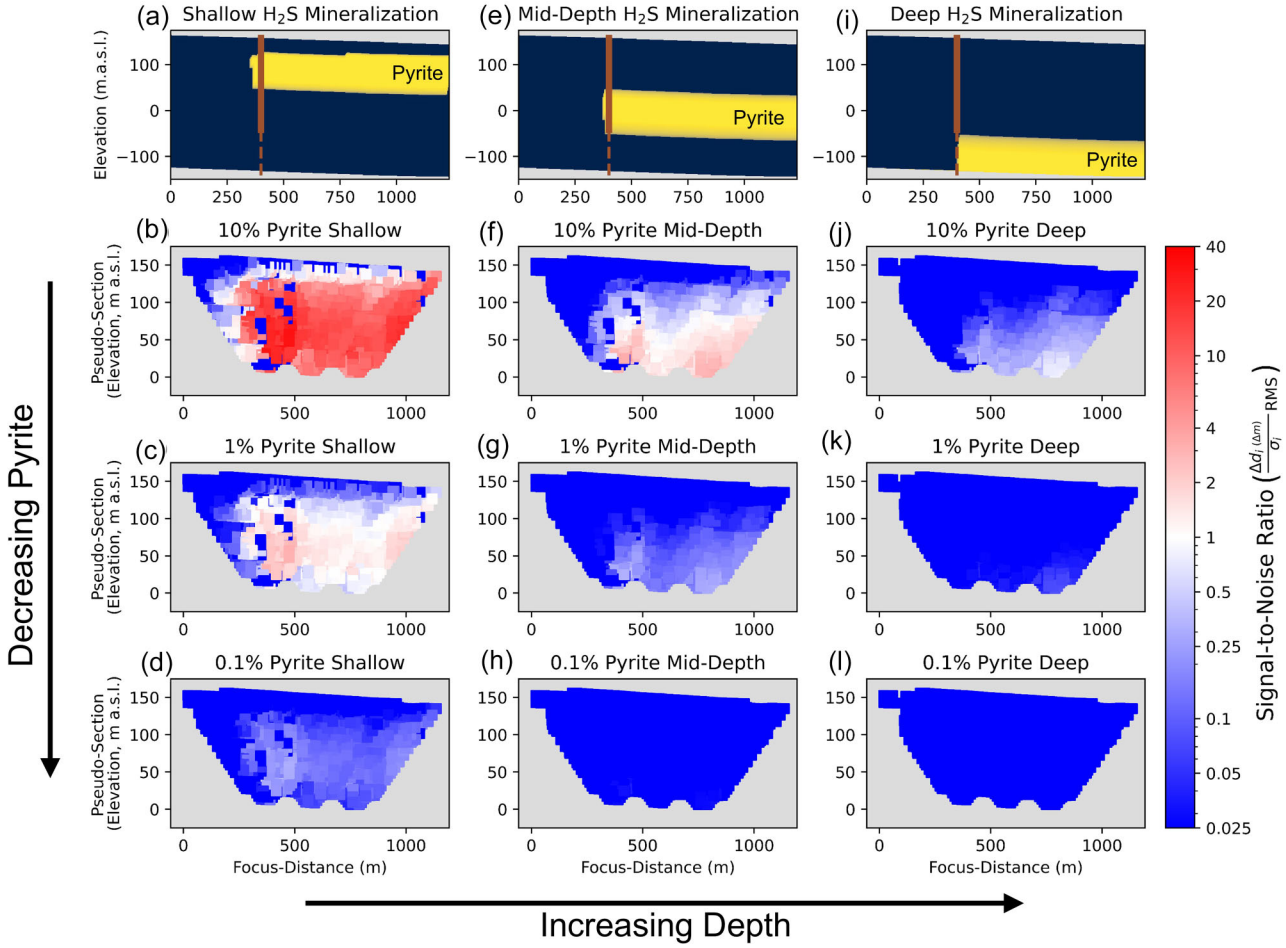

Figure 8. Signal-to-noise ratios of the surface DCIP data to pyrite mineralization at variable depth and abundance. Each column represents the resolution of shallow (a–d), mid-depth (e–h) and deep (i–l) H_2S mineralization, as indicated by the anomaly extent in the top row labeled as pyrite. The second, third and fourth rows are pseudo-sections of the signal-to-noise ratios for chargeability anomalies resulting from 10 per cent, 1 per cent and 0.1 per cent pyrite by volume, respectively. The signal-to-noise ratio is calculated as the root mean square (RMS) of the data variation (Δd_i) across the full IP decay due to the model variation (Δm_j), relative to the data standard deviation (σ_i).

5.2.3 Cross-hole DCIP monitoring

The synthetic 2-D reactive transport models presented in Fig. 7 suggest that cross-hole monitoring could be implemented to monitor long-term H_2S mineralization of highly concentrated H_2S-charged fluids like those injected using the Carbfix method. The downhole electrode configuration in cross-hole surveying enables the imaging of deeper H_2S mineralization that is below the imaging depth of the surface DCIP monitoring. Thus, the method could be applied to enhance the spatial coverage of surface and down-borehole monitoring efforts for H_2S mineral storage (D.A. Ciraula *et al.* 2024; L. Lévy *et al.* 2024b), particularly between the injection and monitoring boreholes.

However, challenges associated with the cross-hole method limit the practicality of cross-hole monitoring for H_2S mineral storage. First, background noise limits the method's ability to quantitatively capture the expected response change at distances greater than 25–50 m from the borehole. While low noise levels (2 per cent) are modelled in this idealized synthetic study, cross-hole surveys can be impacted by complex noise sources that mask the polarization signal, such as geologic noise (J.X. Zhao *et al.* 1986), electrode geometric errors (P.B. Wilkinson *et al.* 2008), electromagnetic coupling (T.P. Gruszka & J.R. Wait 1989; Y. Zhao *et al.* 2015) and cylindrical borehole and casing effects (C.J. Schenkel & H.F. Morrison 1994; B.S. Singer & K.M. Strack 1998; J.L. Osiensky *et al.* 2004). In the case of injection fluid into NN-4 with lower H_2S concentrations, relative to the NJ-18 Carbfix injection, smaller magnitude anomalies make interpretation unreliable and further limit the spatial resolution of the cross-borehole imaging (< 25 m). Secondly, implementing cross-hole surveying can be impractical in the field as it requires nearby boreholes, and the injection infrastructure at the wellhead can impede the ability to place downhole electrodes. Thirdly, shorter timescales, such as monitoring 5 yr of injection (Supporting Information Fig. S6), do not produce a large enough magnitude response change to be resolved by the geophysical inversions, limiting the temporal resolution of cross-hole DCIP monitoring of H_2S mineralization. Lastly, factors other than the pyrite volumetric fraction can potentially impact the field IP response. While many studies show that the chargeability is primarily a function of the metallic particle content (e.g. W.H. Pelton *et al.* 1978; G. Gurin *et al.* 2013, 2015; A. Revil *et al.* 2015; S. Hupfer *et al.* 2016), recent studies have shown varying dependencies of the polarization response of metallic particles on the size of the mineral grains (T. Martin & A. Weller 2023),

geometry and orientation of the mineral grains (S. Izumoto 2023) and state of mineral surfaces (G. Gurin *et al.* 2019). These dependencies may impact the polarization response in the field, as laboratory experiments of H_2S mineralization in basalts recovered various manners of pyrite mineralization (e.g. surface coatings, discrete nodules, intergrowths within other secondary minerals and in fractures within the basaltic glass) (H.T. Schaef *et al.* 2013). Moreover, L. Lévy *et al.* (2024b) observed polarization decreases following an initial increase in wireline DCIP response upon continuous H_2S injection over 540 d at the Nesjavellir site. The author's speculated that this decrease could be caused by a variety of factors, including passivation of the pyrite minerals due to the formation of other secondary minerals (e.g. G. Gurin *et al.* 2019), corrosion of the pyrite surfaces (e.g. E. Placencia-Gómez *et al.* 2013) or connectivity of pyrite grains. Ultimately, these contributions are poorly constrained in the field, and by not considering their potential degradation to the DCIP response, the synthetic cross-hole modelling represents an idealized field scenario. Further processes contributing to the IP response are discussed in the following section.

5.3 Underlying processes contributing to the DCIP response

The results of the DC resistivity and reactive transport modelling can be used to better understand the IP response by detangling the underlying processes that contribute to the IP response in this field setting. The IP resolution is controlled by the signal strength, which depends on the measured subsurface voltages relative to background noise and the magnitude of the chargeability response change. In terms of the IP signal, the reactive transport model and DC resistivity data reveal key factors contributing to weak IP chargeability responses associated with H_2S mineral storage in fractured basalts; (1) the depth at which the mineralization occurs, (2) the widespread distribution of H_2S mineralization and (3) the geological changes occurring alongside H_2S mineralization.

5.3.1 IP Noise sources

Since data quality is a function of the SNR, characterizing data noise is essential to evaluating IP as a monitoring method. The noise distribution is assessed by mapping the average measurement standard deviation along the survey lines, as shown in Supporting Information Fig. S1. The average standard deviations are largest near the infrastructure noise sources, including the buried power line, injection pipes and wells and buildings. The DOI of the DCIP inversions also provides an indirect assessment of data noise, as shallow DOI values indicate data removal and lower parameter sensitivity relative to the noise. As shown in Fig. 6, the DOI values are severely impacted by the infrastructure at the field site. Since this infrastructure is associated with geothermal energy production and H_2S injection, these inherent noise sources potentially limit the broad use of surface DCIP for monitoring H_2S mineral storage at geothermal sites.

5.3.2 H_2S mineralization depth

The depth at which most H_2S mineralization occurs falls well below the DOI recovered in the field data inversions. The induced electrical field is weaker at greater depths, resulting in less current flow and smaller voltage responses. Additionally, the sensitivity to deep structures and the total number of deep data points are limited by the survey line length, requiring large electrode dipole spacings. Large injection currents and long survey lines can be difficult and impractical to implement in the field. This ultimately limits the applicability of surface DCIP as a monitoring tool for H_2S mineralization at Icelandic geothermal reinjection sites, as injection occurs at similar or greater depths than the Nesjavellir wells studied here.

5.3.3 Distribution of H_2S mineralization

The reactive transport model suggests that most of the injected H_2S mineralizes and that mineralization is widespread throughout the injection reservoir. The highly permeable fractured basalt host rock, identified through model calibrations (E. Gómez-Díaz *et al.* 2022; D.A. Ciraula *et al.* 2024) and validated by changes in resistivity observed from 1985 to 2020, is responsible for the widespread distribution of sulfide formation. Since the chargeability is proportional to the volume fraction of metallic minerals (eq. 8), more dilute pyrite mineralization over large total volumes limits the magnitude of the chargeability signal and is one of the largest challenges to using IP as a monitoring tool at Nesjavellir.

5.3.4 Non-Sulfide mineral influences on the IP response

Since the petrophysical relationship in this study relates the chargeability change to the change in metallic particles (iron sulfides and iron oxides), the dissolution of primary iron oxides could mask the chargeability increase from H_2S mineralization. However, the magnetite and ilmenite dissolution is minimal, decreasing the chargeability by less than 0.01 $mV\,V^{-1}$ over 25 yr (Supporting Information Fig. S4). This suggests that these processes are unlikely to influence the measured signal and thus help clarify the geophysical monitoring in terms of reactive processes.

The reactive transport model also suggests that smectite clays precipitate upon basalt alteration. However, the impact of smectite clays on the chargeability response of volcanic rocks is an active area of research (e.g. L. Lévy *et al.* 2018, 2019a, b, c; A. Ghorbani *et al.* 2018; A. Revil *et al.* 2017b, 2015)? One polarization model presented by A. Ghorbani *et al.* (2018) suggests that smectite clays contribute to the background chargeability (m_b) in eq. (7) by:

$$m_b = \frac{D_g \times \lambda \times \mathrm{CEC}}{(\phi \times \sigma_w) + (D_g \times B \times \mathrm{CEC})}, \tag{12}$$

where D_g denotes the grain density (2900 $kg\,m^{-3}$), ϕ is the porosity, σ_w is the fluid conductivity (measured injection fluid conductivity = 0.07 $S\,m^{-1}$ at 25°C), and B and λ denotes two effective ionic mobilities for conduction and polarization (B(Na+, 25 °C) = 3.1×10^{-9} $m^{-2}\,s^{-1}\,V^{-1}$ and λ(Na+, 25°C) = 3.0×10^{-10} $m^{-2}\,s^{-1}\,V^{-1}$) (A. Ghorbani *et al.* 2018; A. Revil & M. Gresse 2021). L. Lévy *et al.* (2018) provides a relationship between the weight fraction of smectites and the CEC measured of CEC = $90.6 \times \mathrm{Wt.Fract.}_{\mathrm{smect.}}$. Using this relationship in eq. (12), the change in smectite content is transformed to an expected chargeability response following 0.5 and 25 yr of H_2S injection. The results find little contribution to the chargeability response from

the CEC of smectite clays (Supporting Information Fig. S4), as anticipated for a system with low-salinity pore fluids and minor smectite content (A. Ghorbani *et al.* 2018).

Alternative polarization models suggest that smectite reduces the IP response due to an increase in electrical conduction through interfoliar current paths in the smectite crystals, reducing the polarization at the fluid–mineral interface (L. Lévy *et al.* 2019a, c). This model is supported by laboratory measurements on geothermally altered Icelandic volcanic rocks, which found that for a given pyrite content, the polarization response (MPA) decreased with increasing smectite content (L. Lévy *et al.* 2019a). Additionally, field DCIP surveys in L. Lévy *et al.* (2019b) found that lower overall resistivities due to smectite clays reduce the measured voltage signals, thereby lowering the SNR and impeding the collection of quality IP data. At Nesjavellir, decreased resistivity values due to warm wastewater injection and subsequent smectite precipitation are apparent between the 1985 and 2020 resistivity data sets. This presents further challenges to resolving H_2S mineralization due to the low SNRs of the surface DCIP survey and the higher temperatures (90°C) and increased alteration near the injection wells for cross-hole DCIP surveying.

5.4 Petrophysical relationships: uncertainties and assumptions

Integrating process-based models with geophysical methods, such as the reactive transport models presented here, relies on the validity of petrophysical relationships. As such, uncertainty in these relationships presents a key challenge to the effective integration of these approaches. For resistivity, future research should focus on refining the relationship between the smectite content, permeability and electrical conductivity (i.e. eq. 10). Laboratory studies on samples with a broader range of permeabilities and degrees of alteration are needed to validate this relationship, particularly for its extrapolation to low smectite contents and high permeabilities, as observed in this study.

For the IP method, numerous studies have demonstrated near-linear relationships, similar to eq. (8), that effectively captures the influence of the concentration of metallic particles on the chargeability (W.H. Pelton *et al.* 1978; S. Nordsiek & A. Weller 2008; G. Gurin *et al.* 2013, 2015; A. Revil *et al.* 2015; S. Hupfer *et al.* 2016; L. Lévy *et al.* 2019a). However, as discussed previously regarding challenges implementing and interpreting cross-hole DCIP monitoring (see the discussion in Section 5.2.3), studies have also suggested a dependence of chargeability on other factors such as the grain size of the metallic particles, mineral type and surface characteristics (e.g. G. Gurin *et al.* 2019; L. Lévy *et al.* 2019a; T. Martin & A. Weller 2023). These additional factors impacting the polarization response, along with uncertainties surrounding the influence of smectite on the polarization response, underscore the need to better constrain the petrophysical relationships associated with the IP geophysical method. Strengthening these relationships and working towards a unified theory of the polarization mechanisms (e.g. M. Bücker *et al.* 2018) will enhance the coupling between the IP responses at the field-scale and the subsurface processes driving them.

6 CONCLUSIONS

This study investigated how field-scale reactive transport modelling can be integrated with electrical geophysics to better understand the process of H_2S mineral storage with both synthetic modelling and a specific application case at the Nesjavellir study site. Through the integration, we assessed, in particular, the ability of time-lapse DCIP to monitor H_2S mineral storage. Time-lapse surface DCIP, collected over 6 months of continuous H_2S injection, did not recover chargeability changes that would indicate H_2S mineralization. The joint interpretation with the reactive transport modelling and the detection limit analysis of the surface DCIP resolution provides insights into the lack of observable chargeability change and reveals that the absence of chargeability change does not necessarily indicate unsuccessful H_2S mineralization at Nesjavellir. Factors contributing to the inability of surface DCIP to monitor H_2S mineralization include total pyrite volume fractions that are too small to produce detectable IP responses, pyrite mineralization occurring too deep (>200 m) for the surface DCIP survey to resolve changes, decreased IP resolution from low resistivities caused by the warm injection water and smectite formation, and high fracture permeability leading to dispersed pyrite formation. While the surface DCIP method cannot monitor H_2S mineralization at the Nesjavellir site, joint reactive transport-DCIP synthetic modelling suggests that cross-borehole DCIP surveying is sensitive to H_2S mineralization at the field-scale. However, the synthetic cross-hole DCIP modelling presented here represents an idealized case (i.e. low data noise, polarization controlled entirely by metallic particle volume content and no degradation of the polarization response from smectite mineralization, pyrite grain geometry or mineral surface passivation), and field implementation of cross-hole DCIP monitoring would require highly concentrated H_2S-rich injection waters (i.e. Carbfix fluids) and long injection durations.

This study also demonstrates how reactive transport modelling can improve the geophysical characterization of the subsurface by constraining the processes underlying the geophysical response. In the low-salinity system at Nesjavellir, the reactive transport model suggests that the polarization response is primarily driven by pyrite mineralization, and the impact of other mineralogical changes associated with basalt alteration, such as iron oxide dissolution and smectite precipitation, is secondary. However, the ability to accurately quantify the impact of smectite formation on the chargeability is limited by uncertainty in the underlying petrophysical relationships. Future studies should prioritize further constraining these relationships and the underlying polarization mechanisms in order to improve the integration of process-based models with IP geophysics.

Since the start of geothermal wastewater disposal at the Nesjavellir site, resistivity decreases from 1925 to 325 Ωm have been identified in the vicinity of the injection wells. These larger conductivities have the potential to further reduce the ability to resolve chargeable structures, such as pyrite mineralization, due to decreased voltage build-up and decreased current density.

Lastly, the observed decrease in resistivity due to warm wastewater disposal was utilized in a petrophysical relationship alongside smectite formation predicted by the reactive transport model to validate the high fracture permeability of 7.9×10^{-12} m^2 in the shallow basaltic reservoir. This integration demonstrates the value that time-lapse geophysics can add to validating reactive transport parameters.

ACKNOWLEDGMENTS

We first thank our editor, Lindsey Heagy, and two anonymous reviewers for their time and constructive feedback that greatly contributed to the presentation and conclusions of this research. Reykjavik Energy and, in particular, Íris Eva Einarsdóttir and Thorsteinn Ari Thorgeirsson, are thanked for providing data on wastewater injection and their support in facilitating and collecting water samples at Nesjavellir. Reykjavik Energy and Iceland GeoSurvey (ÍSOR) are thanked for providing the historic VES data. Pradip Maurya, Muhammad Rizwan Asif, Ásdís Benediktsdóttir and Sigurdur Ymir Richter are thanked for their help with DCIP data collection during the 2020 and 2021 field campaigns. Lydie Gailler and Svetlana Byrdina are also thanked for their participation in the 2019 geophysical field campaign at Nesjavellir, which helped improve the acquisition strategy for the following years. DC thanks Gylfi Páll Hersir for providing valuable insight into the vertical electrical sounding data and data processing. DC also thanks Eric Sonnenthal for help with developing the reactive transport models. Alessandro Signora, Nicole Sullivan and Stefano Galli are thanked for their input and guidance on the use of EEMverter and EEMstudio. General revisions to sentence structure and grammar were supported by AI tools ChatGPT (OpenAI 2025) and Grammarly (Inc. 2025). This project has received funding from the Nordic Volcanological Center (NordVulk), Landsvirkjun Energy Research Fund, the VOR—Reykjavik Energy Research and Innovation Fund and the EEGS Foundation. Funding for the field data collection was provided by the Icelandic Centre for Research (Rannís) to Léa Lévy.

SUPPORTING INFORMATION

Supplementary data are available at *GJIRAS* online.
Please note: Oxford University Press is not responsible for the content or functionality of any supporting materials supplied by the authors. Any queries (other than missing material) should be directed to the corresponding author for the paper.

DATA AVAILABILITY

All geophysical data presented in this study, including the 2020 and 2021 DCIP data sets and the 1985 vertical electrical soundings are available at the following repository, https://doi.org/10.5281/zenodo.15770067, with Creative Commons Attribution 4.0 International license (D.A. Ciraula *et al.* 2026). Geochemical data utilized in the reactive transport modelling can be found at D.A. Ciraula *et al.* (2024), D.A. Ciraula (2025) and D.A. Ciraula *et al.* (in preparation).

REFERENCES

Abdulsamad, F., Florsch, N. & Camerlynck, C., 2017. Spectral induced polarization in a sandy medium containing semiconductor materials: experimental results and numerical modelling of the polarization mechanism, *Near Surf. Geophys.,* **15**(6), 669–683.

Ahmmed, B., Mudunuru, M.K., Karra, S., James, S.C., Viswanathan, H. & Dunbar, J.A., 2020. PFLOTRAN-SIP: A PFLOTRAN module for simulating spectral-induced polarization of electrical impedance data, *Energies,* **13**(24), doi:10.3390/en13246552.

Aradóttir, E.S., Sonnenthal, E.L., Björnsson, G. & Jónsson, H., 2012. Multidimensional reactive transport modeling of CO_2 mineral sequestration in basalts at the Hellisheidi Geothermal Field, Iceland, *Int. J. Greenhouse Gas Control,* **9,** 24–40.

Archie, G.E., 1942. The electrical resistivity log as an aid in determining some reservoir characteristics, *Trans. AIME,* **146,** 54–62.

Arnason, B., Theodorsson, P., Björnsson, S. & Saemundsson, K., 1969. Hengill, a high temperature thermal area in iceland, *Bull. Volcanol.,* **33,** 245–259.

Árnason, K. *et al.*, 1986a. Report OS-87018 (in Icelandic): Nesjavellir - Ölkelduháls Yfirbordsrannsóknir 1986, Orkustofnun, Tech. Rep..

Árnason, K., Johnsen, G.V., Thorbergsson, G., Hersir, G.P. & Georgsson, L.S., 1986b. Report OS-87017 (in Icelandic): Nesjavellir - Jardedlisfrædileg könnun 1985 Mæligögn, Orkustofnun, Tech. Rep..

Arnórsson, S., 1995. Geothermal systems in Iceland: Structure and conceptual models-I. High-temperature areas, *Geothermics,* **24**(5–6), 561–602.

Arnórsson, S., Bjarnason, J.O., Giroud, N., Gunnarsson, I. & Stefánsson, A., 2006. Sampling and analysis of geothermal fluids, *Geofluids,* **6**(3), 203–216.

Auken, E. *et al.*, 2015. An overview of a highly versatile forward and stable inverse algorithm for airborne, ground-based and borehole electromagnetic and electric data, *Explor. Geophys.,* **46**(3), 223–235.

Binley, A., Hubbard, S.S., Huisman, J.A., Revil, A., Robinson, D.A., Singha, K. & Slater, L.D., 2015. The emergence of hydrogeophysics for improved understanding of subsurface processes over multiple scales, *Water Resour. Res.,* **51**(6), 3837–3866.

Bording, T.S., Fiandaca, G., Maurya, P.K., Auken, E., Christiansen, A.V., Tuxen, N., yberg Klint, K.E.S. & Larsen, T.H., 2019. Cross-borehole tomography with full-decay spectral time-domain induced polarization for mapping of potential contaminant flow-paths, *J. Contamin. Hydrol.,* **226,** 103523. doi:10.1016/j.jconhyd.2019.103523.

Briggs, M.A., Day-Lewis, F.D., Ong, J.B., Curtis, G.P. & Lane, J.W., 2013. Simultaneous estimation of local-scale and flow path-scale dual-domain mass transfer parameters using geoelectrical monitoring, *Water Resour. Res.,* **49**(9), 5615–5630.

Bücker, M., Flores-Orozco, A. & Kemna, A., 2018. Electrochemical polarization around metallic particles - part 1: The role of diffuse-layer and volume-diffusion relaxation, *Geophysics,* **83**(4), E203–E217.

Callow, B., Falcon-Suarez, I., Ahmed, S. & Matter, J., 2018. Assessing the carbon sequestration potential of basalt using X-ray micro-CT and rock mechanics, *Int. J. Greenhouse Gas Control,* **70,** 146–156.

Camporese, M., Cassiani, G., Deiana, R., Salandin, P. & Binley, A., 2015. Coupled and uncoupled hydrogeophysical inversions using ensemble Kalman filter assimilation of ERT-monitored tracer test data, *Water Resour. Res.,* **51**(5), 3277–3291.

Carrera, J., Saaltink, M.W., Soler-Sagarra, J., Jingjing, W. & Valhondo, C., 2022. Reactive transport: A review of basic concepts with emphasis on biochemical processes, *Energies,* **15**(3), 925. doi:10.3390/en15030925.

Carrigan, C.R. *et al.*, 2013. Electrical resistance tomographic monitoring of CO_2 movement in deep geologic reservoirs, *Int. J. Greenhouse Gas Control,* **18,** 401–408.

Chen, J., Hubbard, S.S. & Williams, K.H., 2013. Data-driven approach to identify field-scale biogeochemical transitions using geochemical and geophysical data and hidden Markov models: development and application at a uranium-contaminated aquifer, *Water Resour. Res.,* **49**(10), 6412–6424.

Cheng, S.Y. & Hsu, K.C., 2021. Bayesian integration using resistivity and lithology for improving estimation of hydraulic conductivity, *Water Resourc. Res.,* **57**(3), e2020WR027346. doi:10.1029/2020WR027346.

Ciraula, D.A., Fiandaca, G., Chen, J., Scott, S. & Lévy, L., 2026. *Constraining Time-lapse Geophysical Responses with Reactive Transport Modeling: An Approach to Monitor H_2S Mineral Storage [Data set],* Zenodo, https://zenodo.org/records/15770068

Ciraula, D.A., 2025. *Understanding Hydrogen Sulfide Mineral Storage: Joint Geophysical Surveying and Geochemical Modeling at the Nesjavellir Geothermal Site, Iceland,* Ph.D. thesis, Faculty of Earth Sciences, University of Iceland, https://hdl.handle.net/20.500.11815/7964

Ciraula, D.A., Kleine-Marshall, B.I., Galeczka, I.M. & Lévy, L., 2024. Advanced monitoring of H_2S injection through the coupling of reactive transport models and geophysical responses, *Environ. Sci. Technol.,* **58**(25), 11128–11139.

Clark, D.E. *et al.*, 2018. The chemistry and potential reactivity of the CO_2-H_2S charged injected waters at the basaltic CarbFix2 site, Iceland. *Energy Proced.,* **146,** 121–128.

Clark, D.E., Oelkers, E.H., Gunnarsson, I., Sigfússon, B., Snæbjörnsdóttir, S., Aradóttir, E.S. & Gíslason, S.R., 2020. CarbFix2: CO_2 and H_2S mineralization during 3.5 years of continuous injection into basaltic rocks at more than 250°C, *Geochim. Cosmochim. Acta,* **279,** 45–66.

Commer, M., Pride, S.R., Vasco, D.W., Finsterle, S. & Kowalsky, M.B., 2020. Imaging of a fluid injection process using geophysical data - a didactic example, *Geophysics,* **85**(2), W1–W16.

Commer, M., Gasperikova, E. & Doughty, C., 2022. Improved geophysical monitoring of carbon sequestration through parameter linkage to reservoir modeling, *Int. J. Greenhouse Gas Control,* **119,** 103717. doi:10.1016/j.ijggc.2022.103717.

Dahlin, T., Leroux, V. & Nissen, J., 2002. Measuring techniques in induced polarisation imaging, *J. Appl. Geophys.,* **50**(3), 279–298.

Deiana, R., Cassiani, G., Villa, A., Bagliani, A. & Bruno, V., 2008. Calibration of a vadose zone model using water injection monitored by GPR and electrical resistance tomography, *Vadose Zone J.,* **7,** 215–226.

Fiandaca, G., Auken, E., Christiansen, A.V. & Gazoty, A., 2012. Time-domain-induced polarization: full-decay forward modeling and 1D laterally constrained inversion of cole-cole parameters, *Geophysics,* **77**(3), E213–E225.

Fiandaca, G., Ramm, J., Binley, A., Gazoty, A., Christiansen, A.V. & Auken, E., 2013. Resolving spectral information from time domain induced polarization data through 2-D inversion, *Geophys. J. Int.,* **192**(2), 631–646.

Fiandaca, G., Christiansen, A.V. & Auken, E., 2015a. Depth of investigation for multi-parameters inversions, *Near Surf. Geosci.,* **2015,** pp. 1–5. European Association of Geoscientists & Engineers.

Fiandaca, G., Doetsch, J., Vignoli, G. & Auken, E., 2015b. Generalized focusing of time-lapse changes with applications to direct current and time-domain induced polarization inversions, *Geophys. J. Int.,* **203**(2), 1101–1112.

Fiandaca, G., Madsen, L.M. & Maurya, P.K., 2018. Re-parameterisations of the Cole-Cole model for improved spectral inversion of induced polarization data, *Near Surf. Geophys.,* **16**(4), 385–399.

Fiandaca, G. *et al.*, 2023. Closing the gap between galvanic and inductive methods: EEMverter, a new 1D/2D/3D inversion tool for electric and electromagnetic data with focus on induced polarization. Vol. **2023,** pp. 52–66. Australian Society of Exploration Geophysicists Extended Abstracts.

Flores-Orozco, A., Williams, K.H., Long, P.E., Hubbard, S.S. & Kemna, A., 2011. Using complex resistivity imaging to infer biogeochemical processes associated with bioremediation of an uranium-contaminated aquifer, *J. geophys. Res.: Biogeosciences,* **116,** doi:10.5281/zenodo.10052691.

Flores-Orozco, A., Williams, K.H. & Kemna, A., 2013. Time-lapse spectral induced polarization imaging of stimulated uranium bioremediation, *Near Surf. Geophys.,* **11**(5), 531–544.

Foulger, G.R., 1988. Hengill triple junction, SW Iceland: 1. tectonic structure and the spatial and temporal distribution of local earthquakes, *J. geophys. Res.,* **93**(B11), 13493–13506.

Foulger, G.R. & Toomey, D.R., 1989. Structure and evolution of the Hengill-Grensdalur Volcanic Complex, Iceland: geology, geophysics, and seismic tomography, *J. geophys. Res.,* **94**(B12), 17511–17522.

Freeze, R.A. & Cherry, J.A., 1979. *Groundwater,* Prentice-Hall, Inc.

Galeczka, I.M. *et al.*, 2022. A pre-injection assessment of CO_2 and H_2S mineralization reactions at the Nesjavellir (Iceland) geothermal storage site, *Int. J. Greenhouse Gas Control,* **115,** 103610. doi:10.1016/j.ijggc.2022.103610.

Ghorbani, A., Revil, A., Coperey, A., Ahmed, A.S., Roque, S., Heap, M.J., Grandis, H. & Viveiros, F., 2018. Complex conductivity of volcanic rocks and the geophysical mapping of alteration in volcanoes, *J. Volc. Geotherm. Res.,* **357,** 106–127.

Gómez-Díaz, E., Scott, S., Ratouis, T. & Newson, J., 2022. Numerical modeling of reinjection and tracer transport in a shallow aquifer, Nesjavellir Geothermal System, Iceland, *Geotherm. Energy,* **10**(7), doi:10.1186/s40517-022-00217-3.

Government of Iceland, 2010. Regulation no. 5/14/2010. Iceland Ministry of the Environment, Energy and Climate.

Government of Iceland, 2016. Energy, https://www.government.is/topics/business-and-industry/energy/

Gruszka, T.P. & Wait, J.R., 1989. Interaction of induced polarization and electromagnetic effects in borehole probing, *Geoexploration,* **25**(4), 267–277.

Gunnarsson, I. *et al.*, 2018. The rapid and cost-effective capture and subsurface mineral storage of carbon and sulfur at the CarbFix2 site, *Int. J. Greenhouse Gas Control,* **79,** 117–126.

Gurin, G., Tarasov, A., Ilyin, Y. & Titov, K., 2013. Time domain spectral induced polarization of disseminated electronic conductors: Laboratory data analysis through the Debye decomposition approach, *J. Appl. Geophys.,* **98,** 44–53.

Gurin, G., Titov, K., Ilyin, Y. & Tarasov, A., 2015. Induced polarization of disseminated electronically conductive minerals: a semi-empirical model, *Geophys. J. Int.,* **200**(3), 1555–1565.

Gurin, G., Titov, K. & Ilyin, Y., 2019. Induced polarization of rocks containing metallic particles: Evidence of passivation effect, *Geophys. Res. Lett.,* **46**(2), 670–677.

Helgadóttir, H.M., 2021. NN-03 and NN-04 in Nesjavellir: Drill cuttings analysis, ÍSOR Short Report 21001

Hersir, G.P., Árni Gudnason, E. & Flóvenz, Ó.G., 2022. *Geophysical Exploration Techniques,* 2nd edn, vol. **7,** Elsevier.

Hinnell, A.C., Ferré, T.P., Vrugt, J.A., Huisman, J.A., Moysey, S., Rings, J. & Kowalsky, M.B., 2010. Improved extraction of hydrologic information from geophysical data through coupled hydrogeophysical inversion, *Water Resour. Res.,* **46**(4), W00D40. doi:10.1029/2008WR007060.

Hubbard, C.G., West, L.J., Rodriguez-Blanco, J.D. & Shaw, S., 2013. Laboratory study of spectral induced polarization responses of magnetite - Fe^{2+} redox reactions in porous media, *Geophysics,* **79**(1), D21–D30.

Hupfer, S., Martin, T., Weller, A., Günther, T., Kuhn, K., Ngninjio, V.D.N. & Noell, U., 2016. Polarization effects of unconsolidated sulphide-sand-mixtures, *J. Appl. Geophys.,* **135,** 456–465.

Grammarly, 2025. Available at: https://www.grammarly.com

Ívarsson, G., *Niðurrennsli á Nesjavöllum* 2019. Orkuveita Reykjavíkur - Report 2019-0011.

Izumoto, S., 2023. Induced polarization of metal grains: simulations of three-dimensional electric fields, *J. geophys. Res.: Solid Earth,* **128**(9), e2023JB026757. doi:10.1029/2023JB026757.

Jeffery, G.H., Bassett, J., J, M. & Denney, R.C.J., 1989. *Vogel's Textbook of Quantitative Chemical Analysis,* 5th edn, Longman Scientific and Technical.

Jia, N., Wu, C., He, C., Lv, W., Ji, Z. & Xing, L., 2024. Cross-borehole ERT monitoring system for CO_2 geological storage: Laboratory development and validation, *Energies,* **17**(3), 710. doi:10.3390/en17030710.

Kemna, A., Kulessa, B. & Vereecken, H., 2002. Imaging and characterisation of subsurface solute transport using electrical resistivity tomography (ERT) and equivalent transport models, *J. Hydrol.,* **267**(3–4), 125–146.

Kessouri, P. *et al.*, 2019. Induced polarization applied to biogeophysics: recent advances and future prospects, *Near Surf. Geophys.,* **17**(6), 595–621.

Kim, J.H., Yi, M.J., Supper, R. & Ottowitz, D., 2014. Simultaneous inversion of resistivity structure and electrode locations in ERT, in *Near Surface Geoscience 2014-20th European Meeting of Environmental and Engineering Geophysics,* European Association of Geoscientists & Engineers, Athens, Greece.

Lesmes, D.P. & Frye, K.M., 2001. Influence of pore fluid chemistry on the complex conductivity and induced polarization responses of Berea sandstone, *J. geophys. Res.: Solid Earth,* **106**(B3), 4079–4090.

Lévy, L., Gibert, B., Sigmundsson, F., Flóvenz, O.G., Hersir, G.P., Briole, P. & Pezard, P.A., 2018. The role of smectites in the electrical conductivity of active hydrothermal systems: electrical properties of core samples from Krafla volcano, Iceland, *Geophys. J. Int.,* **215**(3), 1558–1582.

Lévy, L., Gibert, B., Sigmundsson, F., Deldicque, D., Parat, F. & Hersir, G.P., 2019a. Tracking magmatic hydrogen sulfur circulations using electrical impedance: Complex electrical properties of core samples at the Krafla volcano, Iceland, *J. geophys. Res.: Solid Earth,* **124,** 2492–2509.

Lévy, L. *et al.*, 2019b. Electrical resistivity tomography and time-domain induced polarization field investigations of geothermal areas at Krafla, Iceland: comparison to borehole and laboratory frequency-domain electrical observations, *Geophys. J. Int.,* **218,** 1469–1489.

Lévy, L., Weller, A. & Gibert, B., 2019c. Influence of smectite and salinity on the imaginary and surface conductivity of volcanic rocks, *Near Surf. Geophys.,* **17**(6), 653–673.

Lévy, L. *et al.*, 2020. Relationships between lithology, permeability, clay mineralogy and electrical conductivity in Icelandic altered volcanic rocks, in *Proceedings World Geothermal Congress*. Available at: https://www.worldgeothermal.org/pdf/IGAstandard/WGC/2020/11093.pdf

Lévy, L. *et al.*, 2022. Quantifying reagent spreading by cross-borehole electrical tomography to assess performance of groundwater remediation, *Water Resour. Res.,* **58,** e2022WR032218. doi:10.1029/2022WR032218.

Lévy, L. *et al.*, 2024a. Managing the remediation strategy of contaminated megasites using field-scale calibration of geo-electrical imaging with chemical monitoring, *Sci. Total Environ.,* **920,** 171013. doi:10.1029/2022WR032218.

Lévy, L., Ciraula, D., Legros, B., Martin, T. & Weller, A., 2024b. Understanding the fate of H_2S injected in basalts by means of time-domain induced polarization geophysical logging, *J. geophys. Res.: Solid Earth,* **129**(6), e2023JB028316. doi:10.1029/2022WR032218.

Loke, M.H., Wilkinson, P.B., Chambers, J.E. & Meldrum, P.I., 2018. Rapid inversion of data from 2D resistivity surveys with electrode displacements, *Geophys. Prospect.,* **66**(3), 579–594.

Madsen, L.M., Fiandaca, G. & Auken, E., 2020. 3-D time-domain spectral inversion of resistivity and full-decay induced polarization data - full solution of Poisson's equation and modelling of the current waveform, *Geophys. J. Int.,* **223**(3), 2101–2116.

Marieni, C., Přikryl, J., Aradóttir, E.S., Gunnarsson, I. & Stefánsson, A., 2018. Towards 'green' geothermal energy: Co-mineralization of carbon and sulfur in geothermal reservoirs, *Int. J. Greenhouse Gas Control,* **77,** 96–105.

Marieni, C., Voigt, M., Clark, D.E., Gíslason, S.R. & Oelkers, E.H., 2021. Mineralization potential of water-dissolved CO_2 and H_2S injected into basalts as function of temperature: Freshwater versus Seawater, *Int. J. Greenhouse Gas Control,* **109,** 103357. doi:10.1016/j.ijggc.2021.103357.

Martin, T. & Weller, A., 2023. Superposition of induced polarization signals measured on pyrite-sand mixtures, *Geophys. J. Int.,* **234**(1), 699–711.

Martin, T., Titov, K., Tarasov, A. & Weller, A., 2021. Spectral induced polarization: frequency domain versus time domain laboratory data, *Geophys. J. Int.,* **225**(3), 1982–2000.

Matter, J.M. *et al.*, 2016. Rapid carbon mineralization for permanent disposal of anthropogenic carbon dioxide emissions, *Science,* **352**(6291), 1312–1314.

Maurya, P.K., Fiandaca, G., Christiansen, A.V. & Auken, E., 2018. Field-scale comparison of frequency- and time-domain spectral induced polarization, *Geophys. J. Int.,* **214**(2), 1441–1466.

McCleskey, R.B., Nordstrom, D.K., Ryan, J.N. & Ball, J.W., 2012. A new method of calculating electrical conductivity with applications to natural waters, *Geochim. Cosmochim. Acta,* **77,** 369–382.

McKelvey, J.G., Southwick, P.F., Spiegler, K.S. & Wyllie, M.R.J., 1955. The application of a three-element model to the S.P. and resistivity phenomena evinced by dirty sands, *Geophysics,* **20**(4), 913–931.

Mellage, A., Holmes, A.B., Linley, S., Vallée, L., Rezanezhad, F., Thomson, N., Gu, F. & Cappellen, P.V., 2018a. Sensing coated iron-oxide nanoparticles with spectral induced polarization (SIP): experiments in natural sand packed flow-through columns, *Environ. Sci. Technol.,* **52**(24), 14256–14265.

Mellage, A., Smeaton, C.M., Furman, A., Atekwana, E.A., Rezanezhad, F. & Cappellen, P.V., 2018b. Linking spectral induced polarization (SIP) and subsurface microbial processes: results from sand column incubation experiments, *Environ. Sci. Technol.,* **52**(4), 2081–2090.

Menke, W., 2018. *Geophysical Data Analysis: Discrete Inverse Theory,* 3rd edn, Elsevier.

Molins, S. & Knabner, P., 2019. Multiscale approaches in reactive transport modeling, *Rev. Mineral. Geochem.,* **85**(1), 27–48.

Muñoz, A.Q., 1996. *Interpretation of Geophysical Well Logs from the Nesjavellir Geothermal Field, Iceland,* Geothermal Training Program (13). , The United Nations University.

Nivorlis, A., Dahlin, T., Rossi, M., Höglund, N. & Sparrenbom, C., 2019. Multidisciplinary characterization of chlorinated solvents contamination and *in-situ* remediation with the use of the direct current resistivity and time-domain induced polarization tomography, *Geosciences,* **9,** 487. doi:10.3390/geosciences9120487.

Nordsiek, S. & Weller, A., 2008. A new approach to fitting induced-polarization spectra, *Geophysics,* **73**(6), F235–F245.

Ntarlagiannis, D., Williams, K.H., Slater, L. & Hubbard, S., 2005. Low-frequency electrical response to microbial induced sulfide precipitation, *J. geophys. Res.: Biogeosciences,* **110**(G2), doi:10.1029/2005jg000024.

Olsson, P.I., Dahlin, T., Fiandaca, G. & Auken, E., 2015. Measuring time-domain spectral induced polarization in the on-time: decreasing acquisition time and increasing signal-to-noise ratio, *J. Appl. Geophys.,* **123,** 316–321.

Olsson, P.I., Fiandaca, G., Larsen, J.J., Dahlin, T. & Auken, E., 2016. Doubling the spectrum of time-domain induced polarization by harmonic de-noising, drift correction, spike removal, tapered gating and data uncertainty estimation, *Geophys. J. Int.,* **207**(2), 774–784.

OpenAI, 2025. ChatGPT, https://chat.openai.com

Osiensky, J.L., Nimmer, R. & Binley, A.M., 2004. Borehole cylindrical noise during hole–surface and hole–hole resistivity measurements, *J. Hydrol.,* **289**(1–4), 78–94.

Palandri, J.L. & Kharaka, Y.K., 2004. A compilation of rate parameters of water-mineral interaction kinetics for application to geochemical modeling, U.S. Geological Survey Open File Report 2004-1068. Available at: https://pubs.usgs.gov/of/2004/1068/pdf/OFR_2004_1068.pdf

Pelton, W.H., Ward, S.H., Hallof, P.G., Sill, W.R. & Nelson, P.H., 1978. Mineral discrimination and removal of inductive coupling with multifrequency IP, *Geophysics,* **43**(3), 588–609.

Peshtani, K., Robinson, J., Torgeson, J., Rabideaux, N., Slater, L. & Qafoku, N.P., 2025. Investigating soil organic matter complexation in natural analog systems using geoelectrical methods, *Environ. Sci. Technol.,* **59**(34), 18203–18212.

Placencia-Gómez, E., Slater, L., Ntarlagiannis, D. & Binley, A., 2013. Laboratory sip signatures associated with oxidation of disseminated metal sulfides, *J. Contamin. Hydrol.,* **148,** 25–38.

Pleasants, M.S., dos A. Neves, F., Parsekian, A.D., Befus, K.M. & Kelleners, T.J., 2022. Hydrogeophysical inversion of time-lapse ERT data to determine hillslope subsurface hydraulic properties, *Water Resour. Res.,* **58**(4), e2021WR031073. doi:10.1029/2021WR031073.

Pollock, D. & Cirpka, O.A., 2012. Fully coupled hydrogeophysical inversion of a laboratory salt tracer experiment monitored by electrical resistivity tomography, *Water Resour. Res.,* **48**(1), doi:10.1029/2011WR010779.

Prikryl, J., Marieni, C., Gudbrandsson, S., Aradóttir, E.S., Gunnarsson, I. & Stefánsson, A., 2018. H_2S sequestration process and sustainability in geothermal systems, *Geothermics,* **71,** 156–166.

Pruess, K. & Narasimhan, T.N., 1985. A practical method for modeling fluid and heat flow in fractured porous media, *Soc. Petrol. Eng. J.,* **25**(1), 14–26.

Rembert, F., 2021. *Development of geo-electrical methods to characterize dissolution and precipitation processes in a carbonate context,* Ph.D. thesis, Sorbonne Université.

Revil, A. & Gresse, M., 2021. Induced polarization as a tool to assess alteration in geothermal systems: A review, *Minerals,* **11**(9), 962. doi:10.3390/min11090962.

Revil, A., Florsch, N. & Mao, D., 2015. Induced polarization response of porous media with metallic particles – Part 1: A theory for disseminated semiconductors, *Geophysics,* **80**(5), D525–D538.

Revil, A., Breton, M.L., Niu, Q., Wallin, E., Haskins, E. & Thomas, D.M., 2017a. Induced polarization of volcanic rocks – 1. surface versus quadrature conductivity, *Geophys. J. Int.,* **208**(2), 826–844.

Revil, A., Murugesu, M., Prasad, M. & Breton, M.L., 2017b. Alteration of volcanic rocks: A new non-intrusive indicator based on induced polarization measurements, *J. Volc. Geotherm. Res.,* **341,** 351–362.

Rubin, Y. & Hubbard, S.S., 2005. *Hydrogeophysics,* vol. **50,** Springer.

Rücker, C., Günther, T. & Wagner, F.M., 2017. pyGIMLi: An open-source library for modelling and inversion in geophysics, *Comput. Geosci.,* **109,** 106–123.

Saneiyan, S., Ntarlagiannis, D., Werkema, D.D. & Ustra, A., 2018. Geophysical methods for monitoring soil stabilization processes, *J. Appl. Geophys.,* **148,** 234–244, doi:

Saneiyan, S., Ntarlagiannis, D., Ohan, J., Lee, J., Colwell, F. & Burns, S., 2019. Induced polarization as a monitoring tool for *in-situ* microbial induced carbonate precipitation (MICP) processes, *Ecolog. Eng.,* **127,** 36–47.

Schaef, H.T., McGrail, B.P., Owen, A.T. & Arey, B.W., 2013. Mineralization of basalts in the CO_2-H_2O-H_2S system, *Int. J. Greenhouse Gas Control,* **16,** 187–196.

Scheibe, T.D. & Chien, Y.J., 2003. An evaluation of conditioning data for solute transport prediction, *Ground Water,* **41**(2), 128–141.

Schenkel, C.J. & Morrison, H.F., 1994. Electrical resistivity measurement through metal casing, *Geophysics,* **59**(7), 1072–1082.

Schmidt-Hattenberger, C., Bergmann, P., ßling, D., Krüger, K., Rücker, C. & Schütt, H., 2011. Application of a Vertical Electrical Resistivity Array (VERA) for monitoring CO_2 migration at the Ketzin site: first performance evaluation, *Energy Proced.,* **4,** 3363–3370.

Scott, S.W. *et al.*, 2023. Valgardur: a database of the petrophysical, mineralogical, and chemical properties of Icelandic rocks, *Earth Syst. Sci. Data,* **15**(3), 1165–1195.

Shuey, R.T., 1975. *Semiconducting Ore Minerals,* vol. **4,** Elsevier Scientific Publishing Company.

Sigfusson, B., Gíslason, S.R. & Meharg, A.A., 2011. A field and reactive transport model study of arsenic in a basaltic rock aquifer, *Appl. Geochem.,* **26**(4), 553–564.

Singer, B.S. & Strack, K.M., 1998. New aspects of through-casing resistivity theory, *Geophysics,* **63**(1), 52–63.

Singha, K. & Gorelick, S.M., 2005. Saline tracer visualized with three-dimensional electrical resistivity tomography: Field-scale spatial moment analysis, *Water Resour. Res.,* **41**(5), doi:10.1029/2004WR003460.

Singha, K., Day-Lewis, F.D., Johnson, T. & Slater, L.D., 2015. Advances in interpretation of subsurface processes with time-lapse electrical imaging, *Hydrol. Process.,* **29,** 6, 1549–1576, doi:

Slater, L.D. & Lesmes, D., 2002. IP interpretation in environmental investigations, *Geophysics,* **67,** 1, 77–88, doi:

Snæbjörnsdóttir, S.O. *et al.*, 2017. The chemistry and saturation states of subsurface fluids during the *in situ* mineralisation of CO_2 and H_2S at the carbfix site in SW-Iceland, *Int. J. Greenhouse Gas Control,* **58,** 87–102.

Snæbjörnsdóttir, S.O., Galeczka, I.M., Sigfússon, B. & Oelkers, E.H., 2021. Injection of geothermal CO_2 and H_2S gases at the Nesjavellir Site, SW Iceland: a pre-injection overview, in *Proceedings World Geothermal Congress*. Available at: https://www.worldgeothermal.org/pdf/IGAstandard/WGC/2020/02054.pdf

Steefel, C.I. & Lasaga, A.C., 1994. A coupled model for transport of multiple chemical species and kinetic precipitation/dissolution reactions with application to reactive flow in single phase hydrothermal systems, *Am. J. Sci.,* **294,** doi:10.2475/ajs.294.5.529.

Steefel, C.I., DePaolo, D.J. & Lichtner, P.C., 2005. Reactive transport modeling: An essential tool and a new research approach for the Earth sciences, *Earth planet. Sci. Lett.,* **240**(3–4), 539–558.

Stefánsson, A., Gunnarsson, I. & Giroud, N., 2007. New methods for the direct determination of dissolved inorganic, organic and total carbon in natural waters by Reagent-Free™ Ion Chromatography and inductively coupled plasma atomic emission spectrometry, *Anal. Chim. Acta,* **582**(1), 69–74.

Stefánsson, A., Arnórsson, S., Gunnarsson, I., Kaasalainen, H. & Gunnlaugsson, E., 2011. The geochemistry and sequestration of H_2S into the geothermal system at Hellisheidi, Iceland, *J. Volc. Geotherm. Res.,* **202**(3–4), 179–188.

Stefánsson, V., 1991. *Fordafrædistudlar: poruhluti bergs,* Orkustofnun Report VS-91/02.

Sullivan, N.A.L., Viezzoli, A. & Fiandaca, G., 2023. EEMstudio: an open-source freeware QGIS plugin for processing, modelling and inversion of electric and electromagnetic data, *Australian Society of Exploration Geophysicists Extended Abstracts,* 8th International Airborne Electromagnetics Workshop, https://zenodo.org/records/10067963

Tran, A.P., Dafflon, B., Hubbard, S.S., Kowalsky, M.B., Long, P., Tokunaga, T.K. & Williams, K.H., 2016. Quantifying shallow subsurface water and heat dynamics using coupled hydrological-thermal-geophysical inversion, *Hydrol. Earth Syst. Sci.,* **20**(9), 3477–3491.

Üner, S., Özürlan Ağaçgözgü, G. & Doğan, D.D., 2019. Hydrogeophysical modelling of Hisarcik (Kütahya) geothermal field, western Turkey, *Geophys. Prospect.,* **67**(8), 2176–2195.

Vinegar, H.J. & Waxman, M.H., 1984. Induced polarization of shaly sands, *Geophysics,* **49**(8), 1267–1287.

Voigt, M., Marieni, C., Clark, D.E., Gíslason, S.R. & Oelkers, E.H., 2018. Evaluation and refinement of thermodynamic databases for mineral carbonation, *Energy Proced.,* **146,** 81–91.

Waxman, M.H. & Smits, L.J., 1968. Electrical conductivities in oil-bearing shaly sands, *Soc. Pet. Eng. J.,* **8**(2), 107–122.

Weller, A. & Slater, L., 2022. Ambiguity in induced polarization time constants and the advantage of the Pelton model, *Geophysics,* **87**(6), E393–E399.

Wilkinson, P.B., Chambers, J.E., Lelliott, M., Wealthall, G.P. & Ogilvy, R.D., 2008. Extreme sensitivity of crosshole electrical resistivity tomography measurements to geometric errors, *Geophys. J. Int.,* **173**(1), 49–62.

Wilkinson, P.B., Meldrum, P.I., Kuras, O., Chambers, J.E., Holyoake, S.J. & Ogilvy, R.D., 2010. High-resolution electrical resistivity tomography monitoring of a tracer test in a confined aquifer, *J. Appl. Geophys.,* **70**(4), 268–276.

Wilkinson, P.B., Uhlemann, S., Chambers, J.E., Meldrum, P.I. & Loke, M.H., 2015. Development and testing of displacement inversion to track electrode movements on 3-D electrical resistivity tomography monitoring grids, *Geophys. J. Int.,* **200**(3), 1566–1581.

Williams, K.H., Ntarlagiannis, D., Slater, L.D., Dohnalkova, A., Hubbard, S.S. & Banfield, J.F., 2005. Geophysical imaging of stimulated microbial biomineralization, *Environ. Sci. Technol.,* **39,** (19), 7592–7600.

Williams, K.H. *et al.*, 2009. Geophysical monitoring of coupled microbial and geochemical processes during stimulated subsurface bioremediation, *Environ. Sci. Technol.,* **43**(17), 6717–6723.

Wong, J., 1979. An electrochemical model of the induced-polarization phenomenon in disseminated sulfide ores, *Geophysics,* **44**(7), doi:10.1190/1.1441005.

Wu, Y., Hubbard, S., Williams, K.H. & Ajo-Franklin, J., 2010. On the complex conductivity signatures of calcite precipitation, *J. geophys. Res.: Biogeosciences,* **115**(G2), doi:10.1029/2009jg001129.

Wu, Y. *et al.*, 2011. Geophysical monitoring and reactive transport modeling of ureolytically-driven calcium carbonate precipitation, *Geochem. Trans.,* **12**(7), doi:10.1186/1467-4866-12-7.

Wu, Y., Surasani, V.K., Li, L. & Hubbard, S.S., 2014. Geophysical monitoring and reactive transport simulations of bioclogging processes induced by leuconostoc mesenteroides, *Geophysics,* **79**(1), doi:10.1190/GEO2013-0121.1.

Wyllie, M. & Southwick, P., 1954. An experimental investigation of the S.P. and resistivity phenomena in dirty sands, *J. Petrol. Technol.,* **6**(2), doi:10.2118/302-g.

Xiao, L., Fiandaca, G., Maurya, P.K., Christiansen, A.V. & Lévy, L., 2022. Three-dimensional time-lapse inversion of transient electromagnetic data, with application at an icelandic geothermal site, *Geophys. J. Int.,* **231**(1), doi:10.1093/gji/ggac206.

Xu, T., Spycher, N., Sonnenthal, E., Zhang, G., Zheng, L. & Pruess, K., 2011. TOUGHREACT version 2.0: A simulator for subsurface reactive transport under non-isothermal multiphase flow conditions, *Comput. Geosci.,* **37**(6), 763–774.

Zarandi, S. & Ivarsson, G., 2010. *A Review on Waste Water Disposal at the Nesjavellir Geothermal Power Plant,* in Proceedings World Geothermal Congress, Available at: https://worldgeothermal.org/pdf/IGAstandard/WGC/2010/0242.pdf

Zhang, B., Engebretsen, K.W., Fiandaca, G., Cai, H. & Auken, E., 2021. 3D inversion of time-domain electromagnetic data using finite elements and a triple mesh formulation, *Geophysics,* **86**(3), doi:10.1190/geo2020-0079.1.

Zhao, J.X., Rijo, L. & Ward, S.H., 1986. Effects of geologic noise on cross-borehole electrical surveys., *Geophysics,* **51**(10), doi:10.1190/1.1442053.

Zhao, Y., Zimmermann, E., Huisman, J.A., Treichel, A., Wolters, B., Waasen, S.V. & Kemna, A., 2015. Phase correction of electromagnetic coupling effects in cross-borehole EIT measurements, *Meas. Sci. Technol.,* **26,** doi:10.1088/0957-0233/26/1/015801.

Zhou, B. & Dahlin, T., 2003. Properties and effects of measurement errors on 2D resistivity imaging surveying, *Near Surf. Geophys.,* **1**(3), 105–117.